A Search for the Higgs boson produced in association with top quarks in multilepton final states at ATLAS

Chris Lester

A DISSERTATION
in
Physics and Astronomy

Presented to the Faculties of The Univeristy of Pennsylvania
in Partial Fulfillment of the Requirements for the Degree of Doctor of Philosophy
2014

Joseph Kroll, Professor, Physics
Supervisor of Dissertation

A.T. Charlie Johnson, Professor, Physics
Graduate Group Chairperson

Dissertation Committee
Randall Kamien, Professor, Physics
I. Joseph Kroll, Professor, Physics
Elliot Lipeles, Assistant Professor, Physics
Burt Ovrut, Professor, Physics
Joseph Kroll, Professor, Physics

A Search for the Higgs boson produced in association with top quarks in multilepton final states at ATLAS

Acknowledgements

Acknowledgements acknowledgements.

Acknowledgements acknowledgements.

Acknowledgements acknowledgements.

ABSTRACT

A Search for the Higgs boson produced in association with top quarks in multilepton final states at ATLAS

Chris Lester

Joseph Kroll

Abstract abstract.

Contents

Preface

This is the preface. Blah blah blah blah blah blah blah. Blah blah blah blah blah blah blah. Blah blah blah blah blah blah blah. Blah blah blah blah blah blah blah. Blah blah blah blah blah blah blah. Blah blah blah blah blah blah blah. Blah blah blah blah blah blah blah. Blah blah blah blah blah blah blah. Blah blah blah blah blah blah blah. Blah blah blah blah blah blah blah. Blah blah blah blah blah blah blah. Blah blah blah blah blah blah blah. Blah blah blah blah blah blah blah. Blah blah blah blah blah blah blah.

Blah blah blah blah blah blah blah. Blah blah blah blah blah blah blah. Blah blah blah blah blah blah blah. Blah blah blah blah blah blah blah. Blah blah blah blah blah blah blah. Blah blah blah blah blah blah blah. Blah blah blah blah blah blah blah. Blah blah blah blah blah blah blah. Blah blah blah blah blah blah blah. Blah blah blah blah blah blah blah. Blah blah blah blah blah blah blah. Blah blah blah blah blah blah blah.

Chris Lester
CERN, Fall 2014

Chapter 1

Introduction

Chapter 2

Theoretical Background

The Standard Model of particle physics (SM) is an extraordinarily successful description of the fundamental constituents of matter and their interactions. Experiments over the past 50 years have verified the extremely precise prediction of the SM. This success has culminated most recently in the discovery of the Higgs Boson. This chapter provides a brief introduction to the structure of the SM and how scientists are able to test it using hadron collider but focuses primarily on the physics of the Higgs boson and its decays to top quarks. Particular attention is given to the importance of a measurement of the rate at which Higgs Bosons are produced in association of top quarks in the context of testing the predictions the SM.

2.1 The Standard Model

2.1.1 The Standard Model Structure

The Standard Model (SM) [1, 2, 3, 4] is an example of a quantum field theory that describes the interactions of all of the known fundamental particles. Particles are understood to be excitations of the more fundamental object of the theory, the field. The dynamics and interactions of the fields are derived from the Standard Model Lagrangian, which is constructed to be symmetric under transformations of the group $SU(3) \times SU(2) \times U(1)$. $SU(3)$ is the group for the color, $SU(2)$ is the group for weak iso spin, and $U(1)$ is the group for weak hyper-charge.

Gauging the symmetries demands the introduction of 8 massless gluons, or the boson (full integer spin) carriers of the strong force [5] from the generators $SU(3)$ symmetry, and the 4 massless bosons, carriers for the weak and electromagnetic forces from the 3 generators of the $SU(2)$ and 1 generator of the $U(1)$ group. The weak and the electromagnetic forces are considered part of a larger single unified electroweak group $SU(2) \times U(1)$ and the associated generators mix.

The gauge symmetry allows the theory to be re-normalizable [6], meaning that unwanted infinities can be absorbed into observables from theory in a way that allows the theory to be able to predict physics at multiple energy scales. Singlets of the $SU(3)$ group are fermions (half-integer spin particles) called leptons and do not interact with the strong, where as doublets of the $SU(3)$ group are called quarks and do interact with the strong force. The SM is a chiral theory: the weak force violates parity, as it only couples to left-chiral particles or right-chiral antiparticles. This means that right-chiral and left-chiral fermions arise from different fields, which are different representations of the weak isospin group.

The discovery of particles and new interactions in various experiments is intertwined with the development of the theory that spans many decades and is not discussed in detail here.

So far, 3 separate generations of both quarks and leptons have been discovered, differing only by mass.The gluon and the 4 electroweak bosons have also been discovered(W^+, W^-, Z^0, and γ) [1]. The reason for this 3-fold replication is not known.

2.1.2 Electoweak Symmetry Breaking and the Higgs

Despite the simple structure of theory, the discovery of massive fundamental particles creates two sets of problems both related to $SU(2) \times U(1)$. First, the force-carrying bosons must enter the theory without mass or the symmetries will be explicitly broken in the Lagrangian. Second, adding fermion masses to theory in an ad-hoc way allows the right-chiral and left-chiral fermions to mix. Since they possesses different quantum numbers, as different representations of the weak-isospin group, this too breaks gauge invariance.

To solve these problems, spontaneous electro-weak symmetry breaking (EWSB) is introduced via the Brout-Englert-Higgs mechanism [7, 8, 9]. A massive scalar field in an electro-weak doublet is added to the theory with 4 new degrees of freedom and a potential which includes a quartic self-interaction term. Each fermion field interacts with the scalar field via a different Yukawa coupling, which unites the left and right chiral fields of a single particle type. This field explicitly preserves all of the symmetries, butt the minimum of the potential does not occur when the expectation of the field is zero. The field eventually falls to a state, where it acquires a vacuum-expectation value. However, a non-zero field must therefore point in a particular direction of weak-isospin space, breaking the symmetry.

[1] The actual particles observed to be produced and propagate may be linear combinations of the underlying generators (for the bosons) or gauge representations (for the fermions).

The consequences of this spontaneous symmetry breaking are tremendous. First, the universe is filled with a field with a non-zero expectation value. The theory can be expanded around this new value and 3 of the degrees of freedom can be interpreted as the longitudinal polarizations of the W^+, W^-, and Z^0, while the 4th remains a scalar field, called the Higgs field with an associated particle called the Higgs particle or "Higgs" The weak bosons acquire a mass via their longitudinal polarizations and the Yukawa couplings of the scalar field to the fermions now behave like a mass term at the this new minimum.

2.1.3 The Standard Model Parameters

Although the SM structure is set by specifying the gauge groups, the EWSB mechanism, and acknowledging the 3-fold replication of the fermions, confronting the SM with experiment requires the measurement of 17[2] free parameters, which are unconstrained from the theory. These free parameters include the fermion masses (from the Yukawa coupling), the force coupling constants, the angles and phase of the mixing between quarks, and constants from the Higgs and electroweak sector[3].

Experiments have provided a number of measurements of the parameters of the SM[10]. Prior to the discovery of the Higgs boson (discussed later) the Higgs mass, however,was the only fully unconstrained parameter, although its value could be inferred via its involvement in loop corrections on the top mass (M_t) and the W mass (M_W). The GFitter collaboration assembles all relevant electroweak observable measurements into a statistical model and then allows certain measurements to float within their uncertainty to allow fora fit among multiple correlated measurements measurements [11]. Figure 2.1 shows the fitted constraints on 4 key SM parameters (M_H, M_W, M_t, $sin^2\theta_w$) with actual measurements overlaid. The addition to the fit of the measured Higgs mass from the ATLAS and CMS collaborations creates a small tension, as the other observables prefer the mass to be much lower ($\sim$ 80 GeV/c^2). The tension in the combined electroweak fit (including the Higgs) is not statistically significant with a p-value of 0.07.

2.2 Collider Physics and the Higgs

To test the theory, physicists accelerate particles to extremely high energies and force them to interact through collisions. Typically, the particles accelerated are electrons or protons, since they are stable.

[2]There are additional parameters from neutrino mass terms and mixing but it is unclear how to include these into the Standard Model, since it does not predict right-chiral neutrinos

[3] The electroweak sector includes parameters like mass of the $W^\pm$ and Z^0 bosons, the weak mixing angle,$sin^2\theta_w$, the fermi constant G_F, and Higgs Mass and vacuum expecation value. These parameters however are not wholly independent. As discussed above, it is only necessary theoretically to specify the two parameters relevant to the Higgs potential and the two coupling associated with the gauge groups

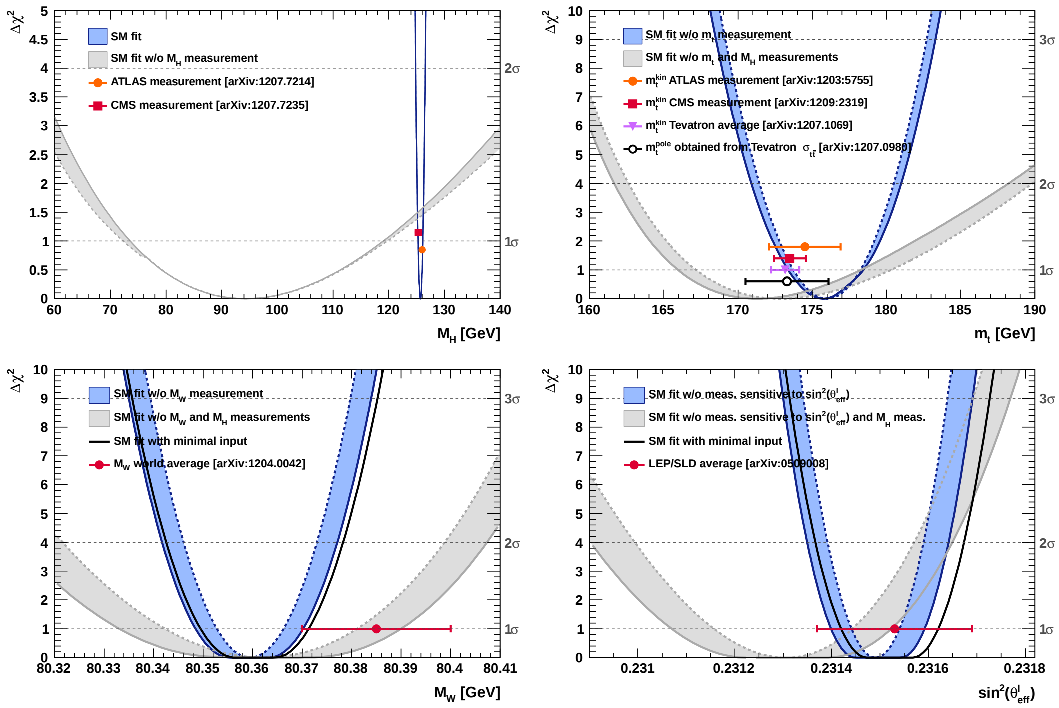

Figure 2.1: χ^2 as a function of the Higgs mass (top left), the top quark mass (top right), the W boson mass (bottom left) and the effective weak mixing angle (bottom right) for the combined SM fit from the GFitter group. The data points placed along $\chi^2 = 1$ represent direct measurements of the respective observable and their $\pm 1\sigma$ uncertainties. The grey (blue) bands show the results when excluding (including) the new M_H measurements from (in) the fits.

Electron-positron collider machines have a rich history of discovery and measurement in particle physics. The advantage of electron accelerators is that the colliding element is itself a fundamental particle. However, due synchrotron radiation, curvature of the beam line becomes problematic for high energy beams. Hadron colliders, specifically, proton-proton and proton-anti-proton colliders can be accelerated in rings without large losses due to synchrotron radiation, but the actual colliding objects at high energies are the constituent quarks and gluons. This complicates analysis because the initial state of the system is not discernible on a per-collision basis and momentum of hard scatter system is unknown along the beam direction.

Collider physics rely on form-factor descriptions of the colliding hadrons that describe the fraction of momentum carried by the hadrons constituent 'partons'. These are called parton-distribution functions, seen in Figure 2.2, and are factorized and integrated through the theoretical calculations of various collision processes [12].

At the Large Hadron Collider or LHC (discussed in detail in Chapter 3 a proton-proton colluder,

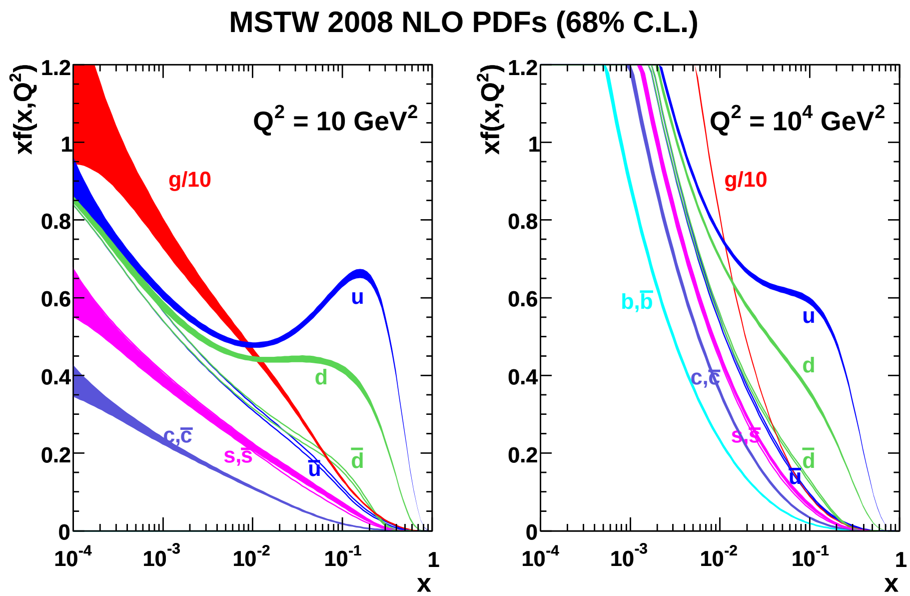

Figure 2.2: Proton Parton Distribution Functions (PDFs) form the MSTW Collaboration at $Q^2 = 10$ GeV^2 and $Q^2 = 10^4$ GeV^2

.

the types of initial states are quark-quark, quark-gluon, and gluon-gluon. Gluon collisions dominate overall, due to the large number of gluons inside the proton, though the relative importance of different initial states changes with the energy scale of the collision and the type of final state sought after.

A prime motivation for the construction of the Large Hadron Collider was the discovery or exclusion of the Higgs boson[13]. LEP and the Tevatron excluded large swaths of possible Higgs boson masses, especially below 114 GeV/$c^2$and the unitarity of certain diagrams including the $WWWW$ vertex required the mass to be below about 1 TeV, a range that was achievable at the LHC with high luminosity running [10].

Despite the ubiquity of Higgs couplings, Higgs boson production at the LHC is a low rate process. Because it couples to fermions proportional to mass and because the colliding particles must be stable and therefore light, production of the Higgs must occur through virtual states.

The Higgs boson can be produced through collision at the LHC via 4 mechanisms: gluon-fusion (ggF), vector-boson fusion (VBF), Higgsstrahlung (VH), and production in association with top quarks ($t\bar{t}H$). The diagrams are shown in Figure 2.3 and the production cross-sections as a function of Higgs mass for the 8 TeV LHC proton-proton runinng are shown in Figure 2.4 [14]. The largest production cross-section is via the gluon fusion channel at 20 pb, which proceeds through a fermion loop that is dominated by the top quark, because of its large Yukawa coupling to the Higgs.

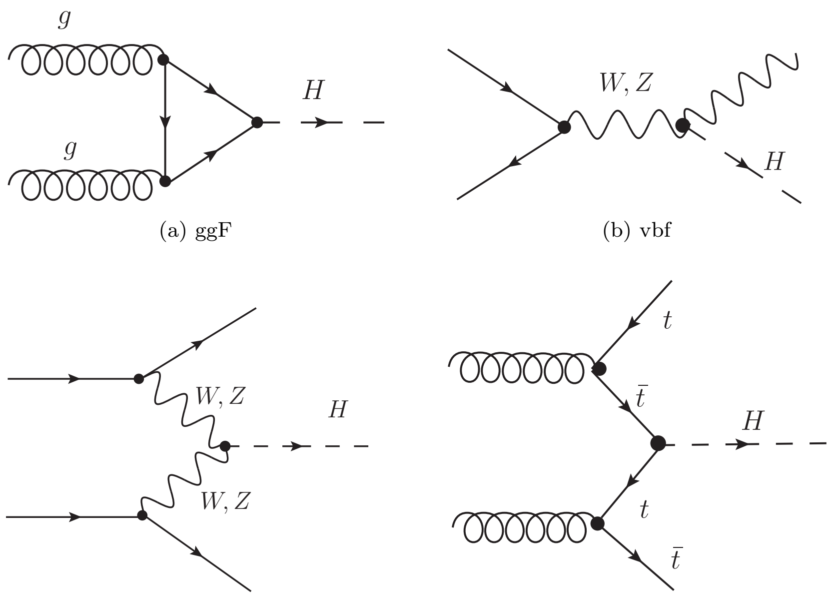

(a) ggF

(b) vbf

(c) vh

(d) $t\bar{t}H$

Figure 2.3: Dominant Higgs production modes at the LHC

Because the Higgs' couples to every massive particle, it has a rich set of decays also seen in Figure 2.4, especially for $m_H = 125$. Studies of Higgs properties at hadron colliders offers many tests of the Standard Model and ample room for searches for new physics. These tests specifically can verify the link between Yukawa coupling and the particles mass and further constrain details of EWSB by examining Higgs coupling to the weak bosons.

2.2.1 Higgs Discovery at the LHC

In 2012 both ATLAS and CMS announced the discovery of a new boson consistent with the Higgs by examining the results of Higgs searches in a number of decay channels ($H \to W^+W^-$,$H \to Z^0Z^0$, and $H \to \gamma\gamma$) in the 2011 dataset at $\sqrt{s}$ =7 TeV and part of the 2012 dataset at $\sqrt{s}$ =8 TeV. By 2013 and 2014, both experiments have updated and/or finalized their results for the full 2011 and 2012 datasets [15, 16]. I will focus on the ATLAS results in the following. The ATLAS measurements constrain both the Higgs mass[17] and spin[18], as well as provide constraints to the Higgs couplings to different particles.

Figure 2.5 show the results of the searches in all of the measurement channels as well as constraints on the SM Higgs coupling parameters in an example fit, where the couplings to the top-quark, bottom-

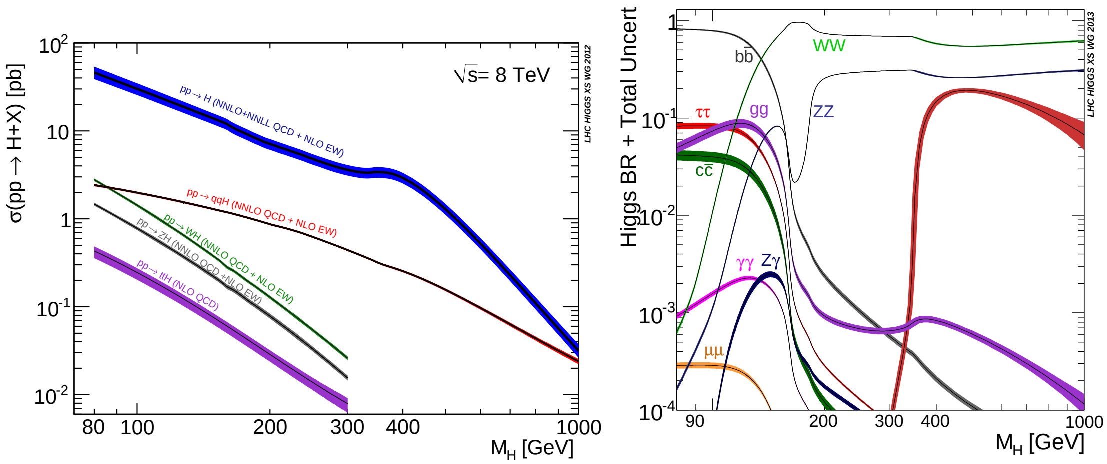

Figure 2.4: 8 TeV LHC Higgs production cross-sections (left) and decay branching fractions

.

quark, W,Z, and τ are allowed to fluctuate independently. These rely on measurements binned in different production and decay channels. They are dominated by higher statistics results in the gluon-fusion production modes, but measurements in the VH and VBF modes are close to SM sensitivity.

The combined results show basic agreement with the SM with much room for improvement with the addition of new production and decay modes and higher statistics. The coupling constraints are particularly strong for the W and Z, which are the most sensitive decay channels, and top quark due to the dominance of the top Yukawa in the ggF loop.

2.2.2 $t\bar{t}H$ Production

Notably absent thus far in the SM are searches for the Higgs in the $t\bar{t}H$ production channel, due to the lack of statistics. Searches are underway and initial results are close to SM sensitivity for ATLAS and CMS. More will be discussed about particular searches later. $t\bar{t}H$ production depends on the top Yukawa coupling at tree level. Comparison of the gluon-fusion and the $t\bar{t}H$ modes would allow for disentangling the effects of of new particles in the gluon-fusion loop[19]. For instance, generic models would allow for the introduction of new colored particles into the loop. The simplest of these models would be the addition of a new generation of quarks. Fourth generation quarks, which obtain mass from a Higgs Yukawa coupling are already largely excluded due to their enormous effects on the Higgs production cross-section[20]. Other exotic scenarios allow for new colored particles in the gluon-fusion loop, which are not entirely constrained by present measurements[21, 22, 23]. These include, for instance, Supersymmetric models involving the stop quark.

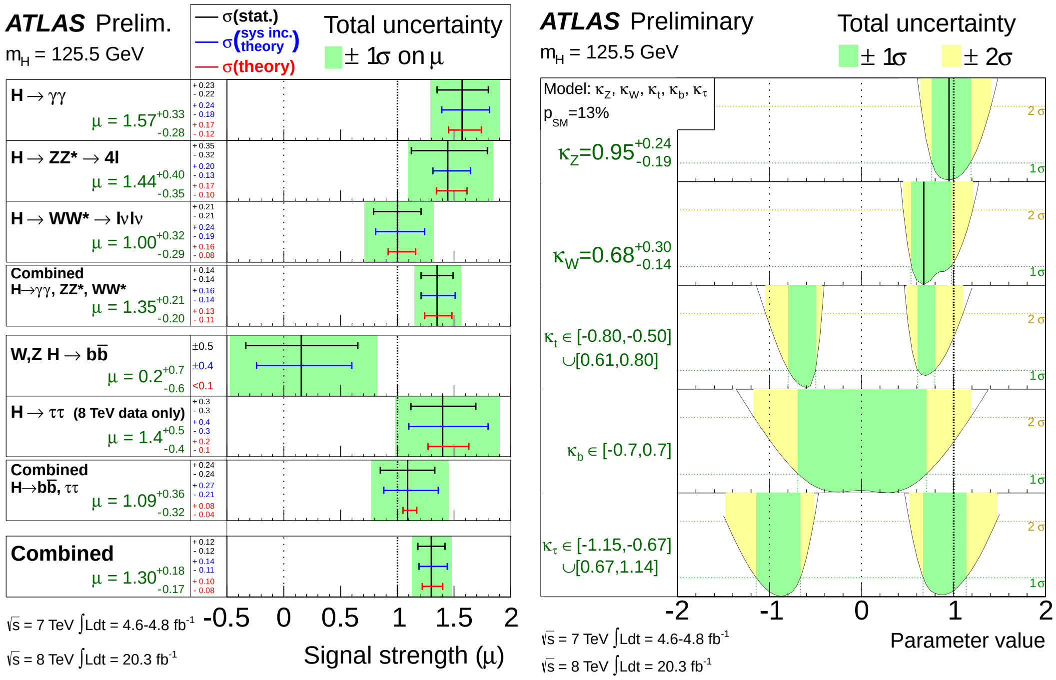

Figure 2.5: ATLAS Higgs combination results for all SM measurement channels as ratios of the measured to SM production cross-sections (left) and extracted Higgs coupling constraint scale-factors for a combined fit to the measurement channels, where the W,Z, top-quark, b-quark, and τ couplings are allowed to float. The p-value of this particular model is 0.13 and in agreement with SM expectations

Aside from the loop effects, measurement of the $t\bar{t}H$ production cross-section would provide a precise measurement of the top Yukawa coupling. When compared with the measured top quark mass, this tests the Higgs mass generation properties for up-type quarks. Despite similar uncertainties on the overall production cross-sections for $t\bar{t}H$ and the gluon-fusion modes, both of which depend on the top Yukawa, most of these uncertainties would cancel for $t\bar{t}H$ if normalized to the topologically similar $t\bar{t}Z$. Finally, the uniqueness of the experimental signature means that searches for $t\bar{t}$ signatures can be performed for a variety of Higgs decays ($\gamma\gamma$, $b\bar{b}$, WW,ZZ, and $\tau\bar{\tau}$ with roughly similar degrees of sensitivity (within a factor of 10)[19].

It is important to note the importance of the top Yukawa coupling to the overall structure of the SM, due to its enormous size compared to other couplings. The top Yukawa is for instance 350000x as large as the electron Yukawa coupling. Because of this the top Yukawa coupling, along with the Higgs mass, is one of the most important pieces of the renormalization group equations (RGE) responsible for the running of the parameter that determines the Higgs self-coupling λ. If this parameter runs negative, then the potential responsible for the entire mechanism of EWSB no longer has a minimum and becomes unbounded, resulting in instability in the universe [24]. Metastability occurs when the

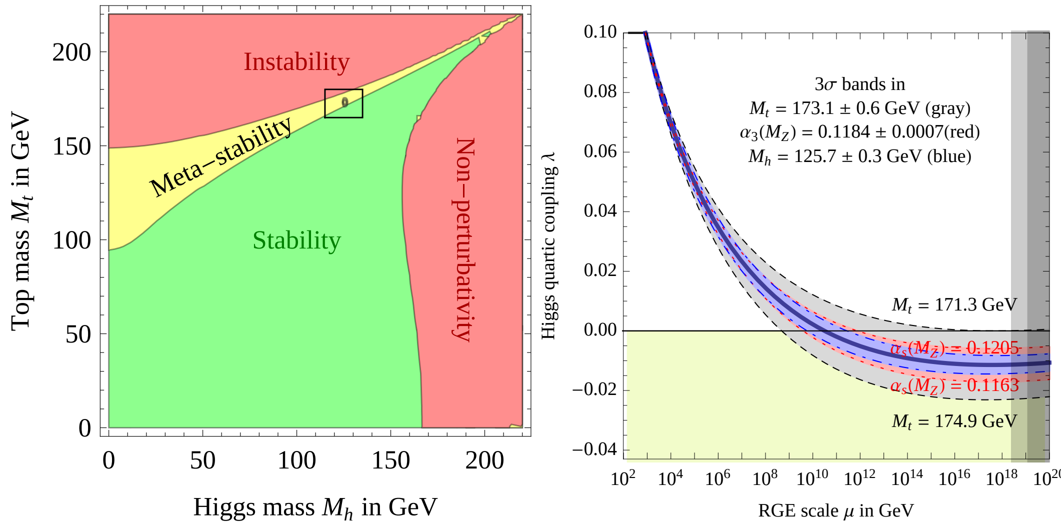

Figure 2.6: RGE for the running of the SM parameter, λ for the Higgs self-coupling term with present values and uncertainty bands for M_H and M_t (left). The two-dimensional plot colored (right) shows regions for which the SM is stable, unstable, and metastable based on this RGE

shape of the potential allows for a false local minimum. Figure 2.6 shows the running of this parameter, the regions for which the universe is stable, unstable and metastable. Current measurements suggest that universe lies in a metastable island[4].

2.3 Conclusion

The Standard Model, despite its success in providing a unified description of fundamental particles and interactions into single theory, has its flaws. These have been discussed in depth elsewhere, but include issues like the description of massive neutrinos, the failure to include gravity, and the unnaturalness of large quantum corrections to Higgs parameters. For these reasons, it seems the SM might be a lower energy approximation to a more fundamental theory. The discovery of the Higgs boson at the LHC provided a stunning verification of one of the fundamental aspects of the theory but at the same time offers new area to search for glimpses of something grander. The production of samples of Higgs bosons allows for a rich array of new tests of the Standard Model, which is now finally over-constrained by experiment. Searches for the $t\bar{t}H$ production, one category of which is the topic of this thesis, provide tree-level access to a central parameter of the theory, the top Yukawa coupling, as well as access a variety of Higgs decays, which will eventually provide a rigorous new test of the SM.

[4]The RGE assumed that there is no new physics at all energy scales

Chapter 3

The Large Hadron Collider and the ATLAS Experiment

3.1 The Large Hadron Collider

Production of a sufficient number of high energy collisions to adequately explore particle physics at the electro-weak scale required the development of one of the most complex machines ever built, the Large Hadron Collider or LHC.

The LHC is the world's highest energy particle accellerator and is located 100m underneath the Franco-Swiss border at the European Organization for Nuclear Research (CERN) in a 26.7 km tunnel.

The technology involved in the development of the LHC and very breifly touched upon in this chapter is an enormous achievement it its own right and is documented in detail here [25, 26, 27].

The LHC is a ciruclar machine capable of accelerating beams of protons and colliding them at center of mass energies up to $\sqrt{s} = 14TeV$ at 4 collision sites around the ring, where 4 experiments are housed (ATLAS[28], CMS[29], LHCb[30], and ALICE[31]. Figure 3.1 is a diagram of the layout of the LHC and its experiments[32]. The LHC also operates in a modes with beams of heavy ions. The LHC is composed of thousands of super-conducting Niobium-Titantium magnets, cooled to 2.7° C with liquid Helium, which steer and focus the particle beams, and a superconducting resonant-frequency (RF) cavity,which boosts the beam to higher energies.

3.1.1 The Accelerator Complex

The accelerator complex is a progressive series of machineswith the LHC as the final stage. Protons are obtained from hydrogen atoms and are accelerated to 50 MeV using the Linac2, before being injected into the Proton-Synchrotron Booster (PSB). In the PSB the protons are accelerated to energies of 1.4

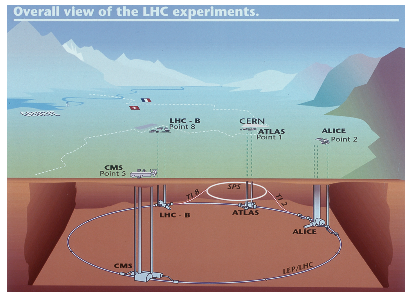

Figure 3.1: Diagram of the Large Hadron collider and location of the 4 main experiments (ATLAS, CMS, LHCb, and ALICE). Around the ring. The diagram also shows the location of the SPS, the final booster ring the accelerator complex that accelerates the protons to 450 GeV before injection into the LHC.

GeV for injection in to the Proton-Synchrotron (PS). The PS accelerates the protons to 25 GeV and dumps bunches into the Super Proton Synchrotron (SPS), where they are accelerated to 450 GeV and finally dumped into the LHC.

3.1.2 Beam Parameters and Collisions

For the physics studied at the ATLAS experiment, the two most important parameters of the collisions provided by the LHC are the center of mass energy and instantaneous luminosity. High center of mass energies are necessary for the production of new high mass particles, and because the consitutents of the actual collisions are the partons of the proton, the CME of the collisions must in general be much higher than the mass of the particles needed to be produced. The

The instantaneous luminosty of the collisions,$\mathcal{L}$, is a measure of the collision rate. The integrated luminosity over time is a measure of the size of the dataset and when multiplied by the cross-section of a particular process gives the total number of expected events produced for that process. Instantaneous luminosity depends on the number of colliding bunches of protons, the intensity of those bunches, the revolution frequency, and the nomralized transvserse spread of the beam in momentum and position phase space, called the emmitance, and the transverse beam size. The LHC has the option for colliding beams with 2808 bunches of protons, each with around $10^{1}1$ protons, at a rate of one bunch collision every 25 ns, or 40 MHz. These correspond to a design luminosity of around $10^{3}4$ cm^{2} s$^{-}1$ or 10 nb$^{-}1$

s^{-}1

Chapter 4

Electrons

4.1 Electrons at Hadron Colliders

4.2 Reconstruction of Electron at ATLAS

4.3 Identification of Electrons at ATLAS

4.3.1 Pile-up

4.3.2 Trigger vs. Offline

4.3.3 2011 Menu

4.3.4 2012 Menu

4.3.5 Electron Likelihood

4.4 Measurement of Electron Efficiency at ATLAS

4.4.1 Techniques

4.4.2 Issues

Chapter 5

Search for the TTH Decay in the Multilepton Channel

This chapter provides an overivew of the the set of analyses searching for the Standard Model (SM) production of the Higgs boson in association with top quarks in multi-lepton final states with multiple jets (including b-quark tagged jets). Searches in $t\bar{t}H$ final states with 2 same-charge, 3 and 4 light leptons (e, μ) are discussed in depth. These final states target specifically Higgs decays to vector bosons, $H \rightarrow W^{\pm}W^{\pm}$ and $H \rightarrow Z^{\pm}Z^{\pm}$ and form a complement to searches for $t\bar{t}H$ production in final states targeting the $H \rightarrow b\bar{b}$ [33], $H \rightarrow \gamma\gamma$[34], and $H \rightarrow \tau\tau$ decay modes.

Based on SM production cross-sections, observation lies just outside the sensitivity of the Run I dataset, even when combining all searches. The analyses provide an opportunity to constrain for the first time the $t\bar{t}H$ production mode with limits reasonably close to the actual production rate. As such the analysis is optimized to overall sensitivty to the $t\bar{t}H$ production rather than individual decay modes, which would be more useful for constraining Higgs couplings.

Detailed description of the event and objection section are provided in Chapter 7, background modelling in Chapter 8, the effect of syetmatic errors and the statistical analysis in Chapter **??** and final results in Chapter **??**.

5.1 Signal Characteristics

$t\bar{t}H$ can be observed in a number of different final states realted to the the Higgs boson and the top quark decay modes.

Three Higgs boson decays are relevant for this analysis: W^+W^- , $\tau^+\tau^-$ and ZZ . The top and anti-top quarks decay in $W^{\pm}b$. Each $W^{\pm}$ boson decays either leptonically (l=$e^{\pm}$, $\mu^{\pm}$,$\tau^{\pm}$) with missing energy or hadronically. Table 5.1 provides the fractional contribution of the main Higgs decay modes at the generator level to $t\bar{t}H$ search channels. These numbers will be modified by lepton acceptances.

Table 5.1: Contributions of the main Higgs decay modes to the 3 multilepton $t\bar{t}H$ signatures at generation level.

Signature	$H \to WW$	$H \to \tau\tau$	$H \to ZZ$
Same-sign	100%	–	–
3 leptons	71%	20%	9%
4 leptons	53%	30%	17%

All modes are generally dominated by the WW signature, though the 3l and 4l channnels possess some contribution from the$\tau\tau$ and ZZ decays.

The signal is expected to be characterized by the presence of 2 b-quark jets from the top quark decays, leptons from vector boson and tau decays, a high jet multiplicity, and missing energy. In general, the number of leptons is anti-correlated with the number of jets, since a vector boson can either decay leptonically or hadronically. For $H \to W^+W^-$, the light quark multiplicity, N_q, and the number of leptons, N_l, follow this relation: $2N_l + N_q + N_b = 10$.

- In the same-sign channel, the $t\bar{t}H$ final state contains 6 quarks. These events are then characterised by a large jet multiplicity.
- In the 3 lepton channel, the $t\bar{t}H$ final state contains 4 quarks from the hard scatter.
- In the 4 lepton channel, the $t\bar{t}H$ final state contains a small number of light quarks, 0 ($H \to W^+W^-$ case), 2 or 4 ($H \to ZZ$ case).

5.2 Background Overview

Background processes can be sorted into two categories:

- Events with a non prompt or a fake lepton selected as prompt lepton. These processes cannot lead to a final state compatible with the signal signature without a misreconstructed object. This category includes events with a prompt lepton but with misreconstructed charge[5]and events

[5]Charge mis-identification is almost exlusively a phenomenon of electrons at our energy scales. While it is is possible for both electrons and muons to have an extremely straight track, whose direction of curvature is difficult to measure, the happens only at extremely high momentum. Electrons on the other hand may interact with the detector material, resulting in bremmstrahlumg. The bremstrahlung photon may subsequently convert resulting in 2 additional tracks near the original electron. This process, called a trident process, may cause a mismatching of the electron cluster with the original electron track and thus a charge-mis identification and happens also at low energies

with jets that "fake" leptons. These processes are rejected with tight object isolation and identification criteria, requiring a large jet multiplicty, and veto-ing events consistent with a leptonically decaying Z boson.

The main backgrounds of this sort are: $t\bar{t}$and Z+jets . Data-driven techniques are used to control some of these processes. Their importance varies depending on the channel.

- Events which can lead to the same final state as the signal (irreducible backgrounds). The main background of this category are: $t\bar{t}V$, $W^{\pm}Z$, and ZZ . They are modeled using the Monte Carlo simulations. In general, these backgrounds are combatted with jet and b-tagged jet requirements. Although the jet multiplicty of $t\bar{t}V$ is high, the multiplicity of $t\bar{t}H$ events is still higher.

5.3 Analysis Strategy

The analysis search is conducted in 3 channels, based on counting of fully identified leptons: 2 SS leptons, 3 leptons,and 4 leptons. The lepton counting occurs before additional object cuts are made in each individual channel to ensure orthoganility. The division into lepton channels rather than channels targeting specific decay modes allows channels with different sensitivities to considered separately. We further divide the 2l SS into sub channels based on the number of jets and flavor of the leptons and the 4l channel into subchannels enriched and depleted in OS leptons arrising from Z decays.

The channels are fed into a posson model

Chapter 6

Dataset and Simulation

6.1 Data

6.1.1 The 2012 Dataset

The LHC successfully produced datasets for physics studies in 2010, 2011 and 2012. The 2012 proton-proton dataset was delivered with collisions with a CME of 8 TeV with bunch collisions every 50 ns and reached a total integrated luminosity of around 20 fb^{-}1 [35]. Figure6.1 shows the accumulation of this dataset over time. Despite doubling the bunch spacing (thereby halving the bunch collision frequency), the lumonisty neared the design lumonisty due to unexpected improvements in the transverse beam profile[36]. This increased the amout of pile-up, or number of collisions per bunch crossing and in general collision events were busier due to these multiple interactions. Figure 6.2 shows the average number of interaction per bunch crossing for the 2011 and 2012 datasets. The 2012 dataset shows an average of 20-25 interactions.

The $t\bar{t}H$ analysis uses the entire 2012 ATLAS dataset, collected from April to December. The size of the dataset corresponds to 20.3 fb^{-1}, after passing data quality requirements, ensuring the proper operation of the tracking, calorimeter and muon subsystems.

The datasets used in the analysis were collected with the primary electron (EF_e24vhi_medium1 —— EF_e60_medium1) and muon triggers (EF_24i_tight —— EF_36_tight). The electron triggers require a electron with at least 25 GeV of calorimeter energy, passing the medium identification requirement and loose tracking isolation. Above 60GeV, the isolation requirement is dropped and the identification is loosened slightly. Similarly, the muon trigger requires a good inner detector track and matching hits in the muon spectrometer, as well as loose tracking isolation, which also is dropped about 36 GeV˙The data sample must contain either a primary muon or primary electron trigger.

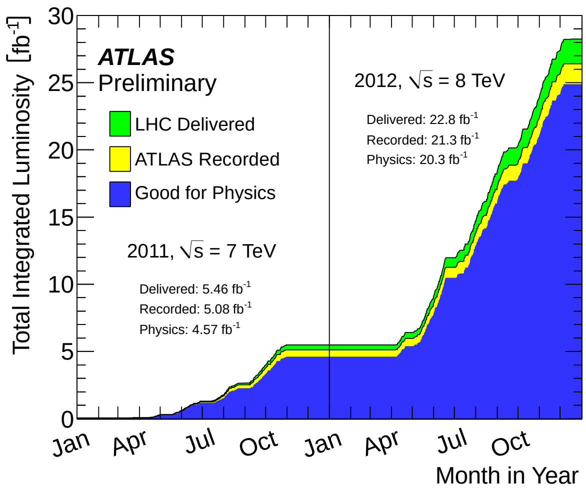

Figure 6.1: Plot showing the accumulation of the integrated lumonisity delivered to the ATLAS experiment over 2011 and 2012. The rough size of the usable, physics ready dataset for 2012 is 20 $fb^{-}1$ and is the dataset used for the following analysis.

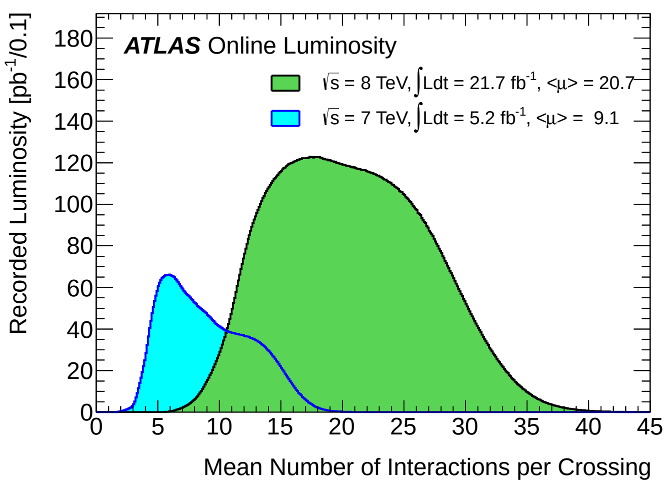

Figure 6.2: The average number of interactions per bunch-crossing for the 2012 and 2011 LHC proton-proton dataset. Most of these interactions are unintersting but leave energetic signatures in particle detectors called pile-up which interfere with measurements

6.2 Simulation

Simulation samples based on are used to determine the overall event selection acceptance and efficiency and for investigations not directly invovled in the final result The simulated samples are created using parton distribution function (PDF) and model using Monte Carlo (MC) techniques the hard parton scatter, underlying event activity and parton showering and hadronization. The samples are then

Table 6.1: Monte Carlo samples used for signal description.

Process	Generator	Cross-section [fb]	$\mathcal{L}$ [fb^{-1}]	Detector simulation
ttH→allhad+H	PowHel+Pythia8	59.09	2146.5	Full
ttH→ljets+H	PowHel+Pythia8	56.63	2238.9	Full
ttH→ll+H	PowHel+Pythia8	13.58	9332.0	Full

passed through a full ATLAS detector simulation[37] based on GEANT4 [38]. Small corrections are then applied to the overall efficiencies to re-scale object identification efficiencies, energy scales, and the pile-up, discussed in depth later.

6.2.1 Signal Simulation

The signal Monte Carlo samples are described in Table 6.1. These large samples are generated with inclusive Higgs boson decays, with branching fractions set to the LHC Higgs Cross Section Working Group (Yellow Report) recommendation for $m_H = 125$ GeV [39]. The matrix element calculation is performed at next-to-leading order (NLO); we use $t\bar{t}H$ Les Houches event format files provided by the authors of the PowHel software [40], decayed and showered with Pythia8[41]. The CT10[42] parton distribution function is used for matrix element generation. The inclusive cross section (129.3 fb at $m_H = 125$ GeV) is also obtained from the Yellow Report [39].

6.2.2 Background Simulation

The background simulations used for this analysis are listed in Table 6.2. In general, the Alpgen[43], MadGraph[44], and AcerMC[45] samples use the CTEQ6L1[46] parton distribution function, while the Powheg[47], Sherpa[48], are generated with the CT10 PDF. The exception is the MadGraph $t\bar{t}t\bar{t}$ sample, which is generated with the MSTW2008 PDF[49]. The highest order calculations available are used for cross sections.

Table 6.2: Monte Carlo samples used for background description. Unless otherwise specified MadGraph samples use Pythia 6 for showering and Alpgen samples use Herwig+Jimmy.

Process	Generator	Detector simulation
$t\bar{t}W^{\pm}$,$t\bar{t}Z$	MadGraph	Full
tZ	MadGraph	AF2
$t\bar{t}t\bar{t}$	MadGraph	Full
$t\bar{t}W^{\pm}W^{\pm}$	Madgraph+Pythia8	AF2
$t\bar{t}$	Powheg+Pythia6	Full/AF2
single top tchan	AcerMC+Pythia6	Full
single top schan→l	Powheg+Pythia6	Full
single top $W^{\pm}t$	Powheg+Pythia6	Full
Wγ*	MadGraph	Full
Wγ+4p	Alpgen	Full
$W^{+}W^{-}$	Sherpa	Full
$W^{\pm}Z$	Sherpa	Full
Same-sign WW	Madgraph+Pythia8	AF2
ZZ→	Powheg+Pythia8,gg2ZZ+Herwig	Full
Zγ*	Sherpa	Full
Z+jets	Sherpa	Full
ggF_H(125)	Powheg+Pythia8	Full

Chapter 7

Object and Event Selection

As stated in Chapter 5, the analysis is divided into 3 signal regions based on lepton counting: 2 same-charge leptons, 3 leptons and 4 leptons. The lepton counting occurs for fully identified leptons with full overlap removal with transverse momentum over 10 GeVto ensure orthoganality. Lepton selections are tightened afterward within each region.

The cuts for each signal region are provided in Table 7.1 and the object selections are detailed in the following selections. The selections are based on optimizations of the region sensitivity performed using MC (event for data driven backgrounds) and adhoc values for normalization systematic errors. All signal regions are comprised of three basic requirements: the presence of b-tagged jets, the presence of additional light jets, and a veto of same flavor opposite sign leptons with an invariant mass within the Z window. Additional requirements on the invariant mass of the leptons, the missing transverse energy in the event, and the total object energy (H_T) proved to have negligble additional benefit at our level of statistics.

7.1 2l Same-Charge Signal Region

The 2 lepton same-charge signal region (2l SS) requires two leptons similar charge. The signal is symmetric in charge but the background from $t\bar{t}$di-lepton production is overwhemling, necessitating the same-sign cut. Requiring only two leptons allows the extra 2 W bosons in the event to decay hadronically, resulting in on average 4 additional light jets plus 2 additional b-quark jets from the top decays.

A leading lepton with transverse momentum of at least 25 GeV/$c$that matches to a trigger and a subleading lepton of at least 20 GeV/c, a b-tagged jet, and at least 4 jets in total are required.

In order to suppress non-prompt backgrounds, the lepton isolation criteria for tracking and

Table 7.1: Selections in the 2l SS, 3l and 4l Signal Regions

Signal Region	2l SS	3l	4l
Trigger Matched Lepton	Yes	Yes	Yes
N_l[6]	=2	=3	=4
Lepton Charge Sum	+2 or −2	+1 or −1	0
Lepton Momentum (GeV/c)[7]	$p_{T0} > 25$ $p_{T1} > 20$	$p_{T0} > 10$ $p_{T1,2}$ >25,20	$p_{T0} > 25$ $p_{T1} > 20$ $p_{T2,3} > 10$
Jet Counting	$N_b \geq 1$, $N_{Jet} = 4$	$N_b \geq 1$, $N_{Jet} \geq 4$ or $N_b \geq 2$, $N_{Jet} = 3$	$N_b \geq 1$, $N_{Jet} \geq 2$
Mass Variables (GeV/c^2)	$\lvert M_{ee} - M_Z\rvert < 10$	$\lvert M_{SFOS} - M_Z\rvert < 10$	$M_{SFOS} > 10$ $150 < M_{4l} < 500$ $\lvert M_{SFOS} - M_Z\rvert < 10$
Sub-channels	2 ($N_{Jet} = 4$, $N_{Jet} \geq 5$) x 3(ee,eμ,$\mu\mu$)	none	2 (No SFOS leps, SFOS leps)

calorimeter are tightened from less than 10% of the lepton momentum to 5%. To suppress charge mis-indentification, the electron is required to be extremely central ($|\eta| < 1.37$) to avoid the material-rich regions of the detector. Additionally, ee events with a lepton pair invariant mass within 10 GeV/$c^2$of the Z pole are removed.

In order to maintain orthoganality with the τ analyses, events with fully identified taus are vetoed.

For the statistical combination the channel is divided into 6 sub-channels: 2 jets counting bins ($N_{Jet} = 4$, $N_{Jet} \geq 5$) x 3 lepton flavor bins (ee,$\mu\mu$,eμ). The splitting allows

7.2 3l Signal Region

The 3 lepton channel requires 3 leptons, whose summed charge is either −1 or +1. The leptons are ordered in this way:

- **l**ep0: the lepton that is opposite in charge to the other two leptons
- **l**ep1: the lepton that is closer in ΔR to lep0
- **l**ep2: the lepton that is farther in ΔR from lep1

Since events with a "fake" lepton arise from di-lepton processes, $t\bar{t}$and Z+jets, where additinal jets are mis-identified as the third lepton, lep0 is never the fake lepton. As a result, the transverse momentum requirement of lep0 is lower that the other two, > 25 GeV/c. For the additional two leptons, one must must match a trigger and have $p_T > 25$ GeV/$c$and the other must have $p_T > 10$ GeV/c.

The 3l channel further requires at least one b-tagged jets and at least 4 jets in total, or two b-tagged jets and exactly 3 jets in total. Additonally, to suppress $W^{\pm}Z$ and Z+jet events, events with same-flavor opposite sign pairs within 10 GeV/$c^2$of the Z pole are vetoed.

Additional cuts, including an $M_l l$ cut, and splittings were investigated but low statistics proved to wash out any advantages.

7.3 4l Signal Region

In the four lepton signal region, selected events must have exactly four leptons with a total charge of zero. At least one leptons with must be matched to one of the applied single lepton trigger. The leading and sub-leading leptons are required to have a $p_{\mathrm{T}}$of 25 and 15 GeV respectively. In order to suppress background contributions from low-mass resonances and Drell-Yan radiation, all opposite-sign-same-flavour (OS-SF) lepton pairs are required to have a dilepton invariant mass of at least 10 GeV.

The four-lepton invariant mass is required to be between 100 and 500 GeV. This choice of mass window suppresses background from the on-shell $Z \to 4\ell$ peak and exploits the high-mass differences between the signal and the dominant $t\bar{t}Z$ background. Events containing an OS-SF lepton pair within 10 GeV of the Z boson mass are discarded. This Z-veto procedure greatly reduces background contributions from ZZ production as well as $t\bar{t}Z$ and while it also affects the signal by vetoing $H \to ZZ^*$, $Z \to \ell^+\ell^-$, these events constitute a small amount of the total expected signal. Finally, selected events are required to have at least two jets, at least one of which must be tagged as a b-quark initiated jet.

The contribution from $t\bar{t}Z$ comprises approximately 75% of the total background in the inclusive signal region. A signal region categorization which factorizes $t\bar{t}Z$ from the remaining backgrounds is thus beneficial. The signal region is accordingly divided into two categories based on the presence of OS-SF lepton pairs in the final state.

7.4 Electron Selection

The electrons are reconstructed by a standard algorithm of the experiment [50] and the electron cluster is required to be fiducial to the barrel or endcap calorimeters: $|\eta_{cluster}| < 2.47$. Electrons in the transition region, $1.37 < |\eta_{cluster}| < 1.52$, are vetoed. Electron reconstruction and identification is discussed in depth in Chapter 4 Electrons must pass the the VeryTight likelihood identification criteria.

In order to reject jets (b-quark jets in particular) misidentified as electrons, electron candidated must also be well isolated from additional tracks and calorimeter energy around the electron cluster. Both the tracking and calorimeter energy within $\Delta R = 0.2$ of the electron cluster must be less than 5% of the electron transverse momentum: $ptcone20/P_t < 0.05$ and $Etcone20/E_T < 0.05$. All quality tracks with momentum greater than 400 MeV contribute to the isolation energy. Calorimeter isolation energy is calculated using topological clusters with corrections for energy leaked from the electron cluster. Pile-up and underlying event corrections are applied using a median ambient energy density correction.

The electron track must also match the primary vertex. The longitudinal projection of the track along the beam line, $z0 \sin\theta$, must be less than 1 cm) and the transverse projection divided by the parameter error, $d0$ significance,must be less than 4. These cuts are used in particular to suppress backgrounds from conversions, heavy-flavor jets and electron charge-misidentifications.

The electron selection is provided in Table 7.2.

7.5 Muon Selection

Muons used in the analysis are formed by matching reconstructed inner detector tracks with either a complete track or a track-segment reconstructed in the muon spectrometer (MS). The muons must satisify $|\eta| < 2.5$. The muon track are required to be a good quality combined fit of inner detector hits and muon spectrometer segments, unless the muon is not fiducial to the inner detector, $|\eta| > 2.4$. Muons with inner detector tracks are further required to pass standard inner detector track hit requirements [51].

As with electrons, muons are required to be isolated from additional tracking or calorimeter energy: $ptcone20/P_t < 0.1$, $Etcone20/E_T < 0.1$) A cell-based $Etcone20/P_T$ relative isolation variable is used. A pile-up energy subtraction based on the number of reconstructed verticies in the event is applied. The subtraction is derived from a Z boson control sample.

The muons must also originate from the primary vertex and have impact parameter requirements, $d0$ significance < 3, and $z0 \sin\theta < 0.1$ cm, similar to the electrons.

The muon selection is provided in Table 7.2.

7.6 Jet and b-Tagged Jet Selection

Jets are reconstructed in the calorimeter using the anti-k_t [52] algorithm with a distance parameter of 0.4 using locally calibrated topologically clusters as input (LC Jets).

Jets must pass loose quality requirement,ensuring the proper functioning of the calorimeter at the time of data taking. Jets near a hot Tile cell in data periods B1/B2 are rejected. The local hadronic calibration is used for the jet energy scale, and ambient energy corrections are applied to account for energy due to pileup.

p_{T} and η cuts are tuned based on the sensitivity to $t\bar{t}H$.

For jets within $|\eta| < 2.4$ and $p_T < 50$ GeV, are required to be associated with the primary vertex, the "jet vertex fraction" (or JVF), which is the fraction of track p_T associated with the jet that comes from the primary vertex, must exceed 0.5 (or there must be no track associated to the jet).

B-jets are tagged using a Multi-Variate Analysis (MVA) method called MV1 and relying on information of the impact parameter and the reconstruction of the displaced vertex of the hadron decay inside the jet.The output of the tagger is required to be above 0.8119 which corresponds to a 70% efficient Working Point (WP).

7.7 Tau Selection

The tau selection is important only in the 2l SS channel, due the tau veto to ensure orthoganality with analyses searching for tau final states for a future combination.

7.8 Object Summary and Overlap

7.9 Optimization

Parameter	Values	Remarks
	Electrons	
p_{T}	> 10 GeV	
$\|\eta\|$	< 2.47 veto crack	< 1.37 for 2l SS channel
ID	Very Tight Likelihood	
Isolation	$E_{\mathrm{T}}Cone20/p_{\mathrm{T}}$,$p_{\mathrm{T}}Cone20/p_{\mathrm{T}} < 0.05$	
Jet overlap removal	$\Delta R > 0.3$	
$\|d_0^{sig}\|$	$< 4\sigma$	
$z_0 sin\theta$	< 1 cm	
	Muons	
p_{T}	> 10 GeV	
$\|\eta\|$	< 2.5	
ID	Tight	
Jet overlap removal	$\Delta R > 0.04 + 10$ GeV$/p_T$	
Isolation	$E_{\mathrm{T}}Cone20/p_{\mathrm{T}}$,$p_{\mathrm{T}}Cone20/p_{\mathrm{T}} < 0.1$	< 0.05 for 2 leptons
$\|d_0^{sig}\|$	$< 3\sigma$	
z_0	< 1 cm	
	Taus	
p_{T}	> 25 GeV	
ID	Medium BDT	
Isolation		
Jet overlap removal	$\Delta R > 0.3$	
e/μ vetoes	Medium electron veto	
	Jets	
p_{T}	> 25 GeV	
$\|\eta\|$	< 2.5	
JVF	JVF> 0.5 or no associated track or $p_{\mathrm{T}}> 50$ GeV	
b-Tag	MV1 70% operating point	

Table 7.2: Object identification and selection used to define the 5 channels of the multilepton $t\bar{t}H$ analysis. Some channels use a sub-sample of objects as precised in the *R*emarks column.

Chapter 8

Background Estimation

The $t\bar{t}H$ multi-lepton signal regions discussed in Chapter 5 are contaminted by background contributions at a similar order of magnitude to the signal. The dominant background for each region is vector boson production in association with top quarks ($t\bar{t}V$). Sub-dominant but important backgrounds include the production of vector boson pairs in associated with jets and b-quark jets (VV) and $t\bar{t}$production with a jet misidentified as a lepton (fakes). The 2l SS regions possesses a unique background of charge misidentification from Z and top events. The methods for estimating these backgrounds are discussed in this chapter. Monte Carlo simulation is used for the prompt $t\bar{t}V$ and VV contributions. Systematic uncerainties on the overall normalization of these backgrounds in the signal region are provided from theoretical studies and past ATLAS analyses and are verified in data-based validation regions. The non-prompt backgrounds from $t\bar{t}$jet-misidentification and charge-misidentification are estimated using data-driven methods.

For reference, Table **??** provides a summary of the $t\bar{t}H$ signal and background expectation for each of the signal regions, including the data-driven estimates discussed in this section. For each region, the background contribution exceeds the size of the signal.

8.1 Vector Boson ($W^{\pm}$, Z) production in association with top quarks: $t\bar{t}V$, tZ

This section describes the estimation and $t\bar{t}V$ productions. Production of top quarks plus vector boson is an important background in all multilepton channels. A large part of the $t\bar{t}V$ component, arising from on-shell $Z \rightarrow \ell\ell$, can be removed via a Z mass veto on like-flavour, opposite sign leptons. However the $Z \rightarrow \tau\tau$ and γ^* components remain. The $t\bar{t}W^{\pm}$ and tZ processes generally require extra jets to reach the multiplicity of our signal regions. Uncertainties from the choice of the factorization

Table 8.1: NLO cross section and theoretical uncertainty calculations derived from MadGraph5_aMC@NLO.

Process	σ_{NLO} $[fb]$	Scale Uncertainty [%]		PDF Uncertainty [%]		Total symmetrised uncertainty [%]
$t\bar{t}W^+$	144.9	+10	-11	+7.7	-8.7	13.3
$t\bar{t}W^-$	61.4	+11	-12	+6.3	-8.4	13.6
$t\bar{t}Z$	206.7	+9	-13	+8.0	-9.2	14.0
tZ	160.0	+4	-4	+7	-7	8.0
$\bar{t}Z$	76.0	+5	-4	+7	-7	8.6

(μ_{F}) and renormalisation μ_{R} scales as well as from the PDF sets are considered evaluating their impacts on both the production cross sections and on the event selection efficiencies (particularly resulting from effects on the shape of number of jets spectrum).

Monte Carlo events for these processes are generated with MadGraph 5 and showered with Pythia 6. $t\bar{t}W^{\pm}$ events are generated with up to two extra partons at matrix element level, while for $t\bar{t}Z$ up to one extra parton at matrix-element level is produced. The tZ process is simulated without extra partons. The next-to-leading-order (NLO) cross sections are implemented by applying a uniform k-factor to the leading-order (LO) events for each process. For $t\bar{t}Z$, there is a large component of off-shell production, and for the 3 and 4 ℓ channels low mass $\gamma^*/Z \rightarrow \ell\ell$ is an important background after on-shell production is removed with a Z veto. In this case the k-factor is determined by comparing LO and NLO cross sections for on-shell Z production only.

The $t\bar{t}V$ uncertainties are calculated using the internal QDC scale and PDF reweighting that is available with MadGraph5_aMC@NLO. The prescription for the scale envelope is taken from [53]: the central value $\mu = \mu_R = \mu_F = m_t + m_V/2$ and the uncertainty envelope is $[\mu_0/2, 2\mu_0]$. The PDF uncertainty prescription used is the recipe from [54]: calculate the PDF uncertaintly using the MSTW2008nlo [49] PDF for the central value and then the final PDF uncertainty envelope is derived from three PDF error sets each with different α_S values (the central value and the upper and lower 90% CL values). The final NLO cross section central values and uncertainties are given in Table 8.1.

The tZ process is normalized to NLO based on the calculation in Ref. [55]. Here the scales are set to $\mu_0 = m_t$ and the scale variations are by a factor of four; the scale dependence is found to be quite small.

8.1.1 $t\bar{t}Z$ Validation Region

Unlike $t\bar{t}W^{\pm}$, a $t\bar{t}Z$ validation region can be obtained by simply inverting the veto on same-flavor opposite sign lepton pairs near the Z pole in the 3 lepton signal region. This region thus requires 3 leptons (with momentum and identification cuts discussed in Chapter 7, at least one opposite sign, same-flavor pair of leptons within 10 GeV/$c^2$of the Z mass, and either 4 jets and at least 1 b-tagged jet or exacly 3 jet and 2 or more b-tagged jets. The resulting region has low statistics and is not used as a control region but is instead used as a validation to demonstrate that the normalization uncertainty, discussed above, is properly evaluated.

The region defined by this is predicted to be 67% $t\bar{t}Z$, 17% WZ, and 13% tZ . We predict 19.3 ± 0.5 events and observe 28, giving a observed-to-predicted ratio of $1.45 \pm 0.27 \pm 0.03$ (where the errors are from data and simulation statistics, respectively).Given the large errors, the region is still in agreement with the predictions to within 1-1.5 σ. Distributions of various variables are shown in Fig. 8.1.

8.2 Di-boson Background Estimation: $W^{\pm}Z$,ZZ

$W^{\pm}Z$ and ZZ di-boson production with additional and b-tagged jets constitute small contributions to the 3- and 4-lepton channels respectively. In the 3-lepton case $W^{\pm}Z$ comprises $\sim$ 1 event of $\sim$ 10 total background events while the ZZ contribution accounts for approximately 10% of the total background in the 4-lepton channel. Because of the small size of these contributions, each of the above processes can be assigned a non-aggressive uncertainty based on similar previous analyses with ATLAS and cross-checked with data validation regions and MC truth studies. We assign an overall 50% error on both the $W^{\pm}Z$ 3-lepton signal region contribution and the ZZ 4-lepton signal region contribution. The details of this error assignment are discussed below.

Both $W^{\pm}Z$ and ZZ production have been studied by ATLAS [56][57] but neither process has been investigated thoroughly in association with multiple jets and b-quark jets. However, both $W+b$ [58] and $Z+b$ [59] production in 7 TeV data have been shown to agree with MC models to within 20-30%. A single W produced in association with b-tagged jets possesses a similar topology to the $W^{\pm}Z+b$ process at a different energy scale and has been shown to be dominated by charm mis-tags and b-jets from gluon splitting and multiple parton interaction. The $W+b$ analysis unfortunately uses Alpgen MC with Herwig PS modeling and only provides results to 1 additional jet and therefore is not directly applicable to this $t\bar{t}H$ analysis (where $W^{\pm}Z$ is modeled using Sherpa with massive c and b quarks). $Z+b$ production originates from slightly different diagrams than $ZZ+b$ however

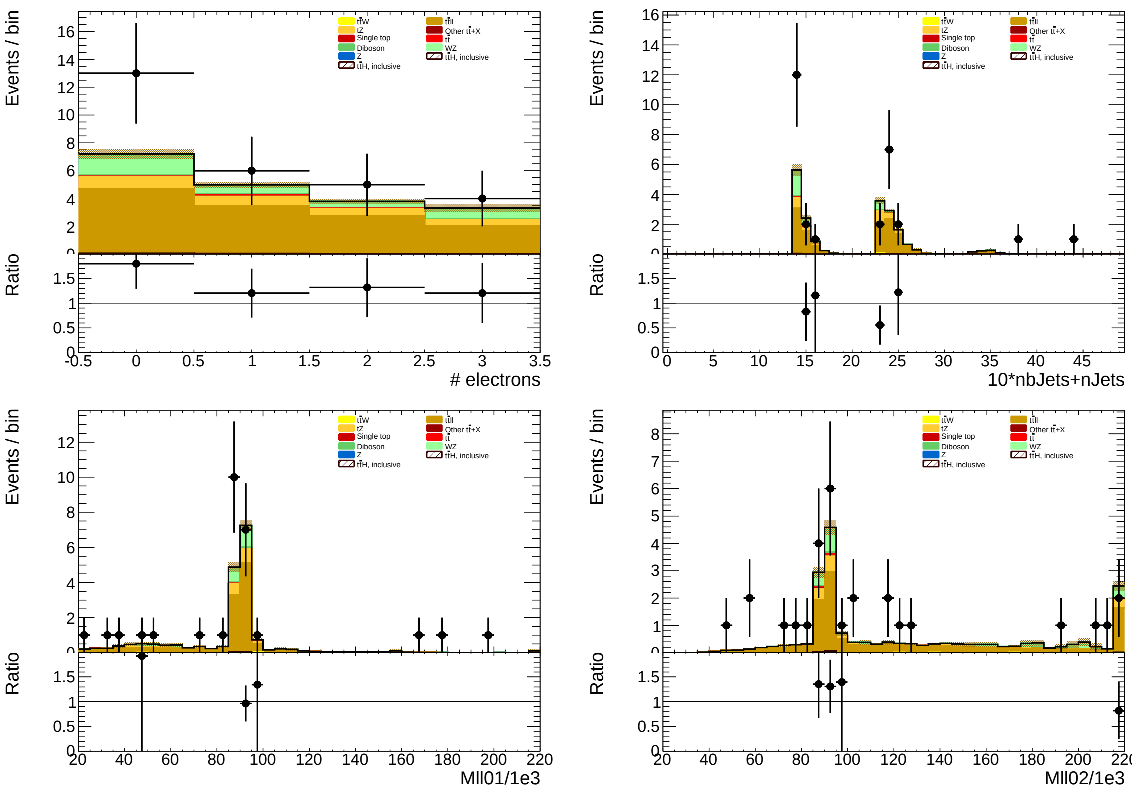

Figure 8.1: Data/MC comparison plots for $t\bar{t}Z$ control region A (≥ 4 jets, ≥ 1 b-tag and 3 jets, ≥ 2 b-tag). In all plots, the rightmost bin contains any overflows. Top left: number of electrons. Top right: 10*the number of b-tags + the total number of jets. Middle left: the invariant mass of the (0,1) lepton pair (see the text for the definition of the lepton ordering). Middle right: the invariant mass of the (0,2) lepton pair.

the sources of the b-tags are similar and the analysis above provides results with Sherpa MC with an agreement of $\sim 30\%$.

In the following two sections the uncertainty assignments for each of these two di-boson processes will be reviewed in turn.

8.2.1 $W^{\pm}Z$ Uncertainty

The $t\bar{t}H$ analyses has two validation regions to test the Sherpa agreement with data for $W^{\pm}Z$: one inclusive 3 lepton region, using the three-lepton channel object and p_{T} cuts; and a $W^{\pm}Z + b$ region with 1 b-tagged jet, fewer than 4 jets (to remove $t\bar{t}V$), and a requirement that at least one same-flavor opposite sign pair have an invariant mass within 10 GeV/$c^2$of the Z mass. Figure 8.2 shows kinematic varibles for the inclusive region [8]. The NJet spectrum shows good agreement within statistics across the full spectrum, giving confidence about the Sherpa high NJet SR extrapolation. Figure 8.3 shows NJet spectrum for the $W^{\pm}Z+b$ validation region with good agreement in the 1 and 2 jet bins, but a slight data-MC discrepancy in the 3 jet bin. The region has low stats and around $\sim 60\%$ purity.

We assign a conservative 50% systematic error to cover MC modeling based on these distributions and the agreement seen in similar $W+b$ and $Z+b$ analyses and use the MC central value for the final $W^{\pm}Z$ in the SR.

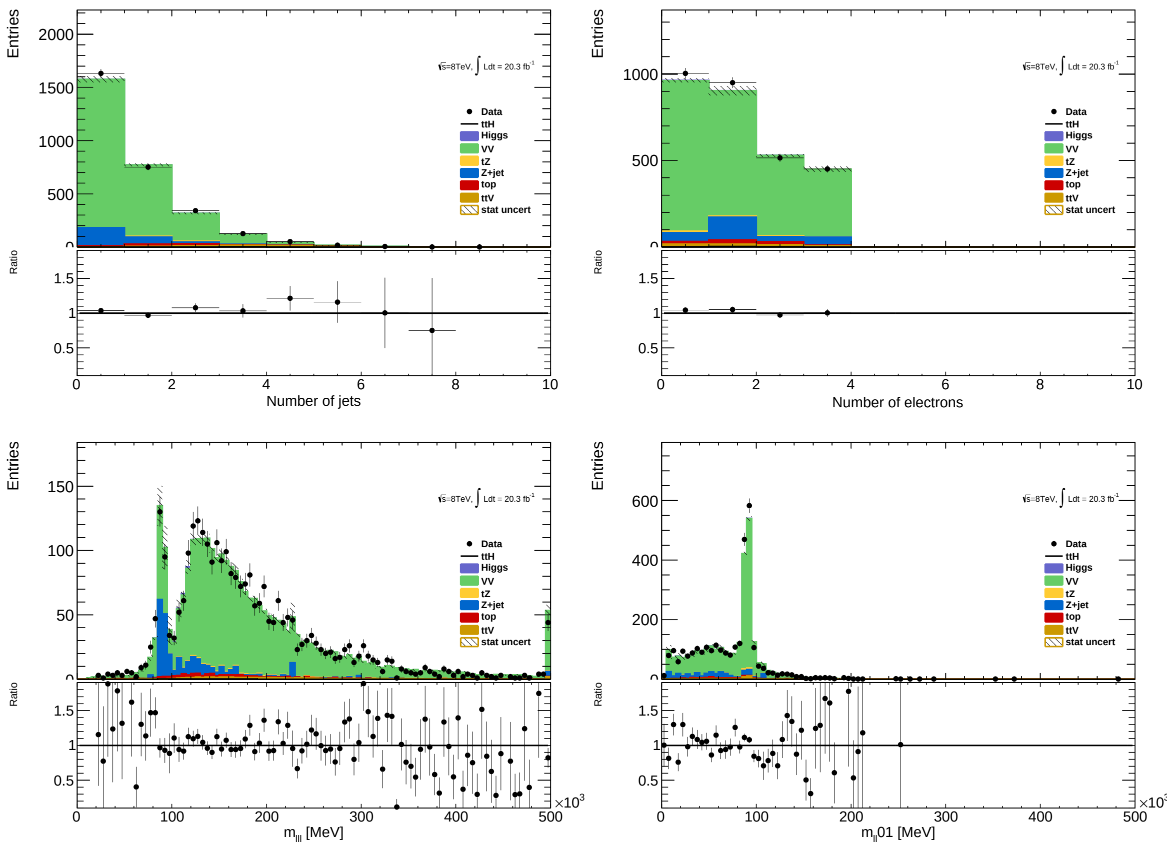

Figure 8.2: Inclusive 3 lepton $W^{\pm}Z$ validation region using the $t\bar{t}H$ lepton identification and momentum cuts: mass, number of jet and flavor variables

A cross-check is undertaken by examining the $W^{\pm}Z$ truth origins of the b-jet in the $W^{\pm}Z+b$ validation region (VR) and the signal region using the sherpa sample available. Table 8.2 shows these fractions. As expected the charm and b contributions dominate, though there is a small dependence on the number of jets. The composition of the VR is fairly similar to that of the signal region, especially

[8]the fakes are taken directly from MC

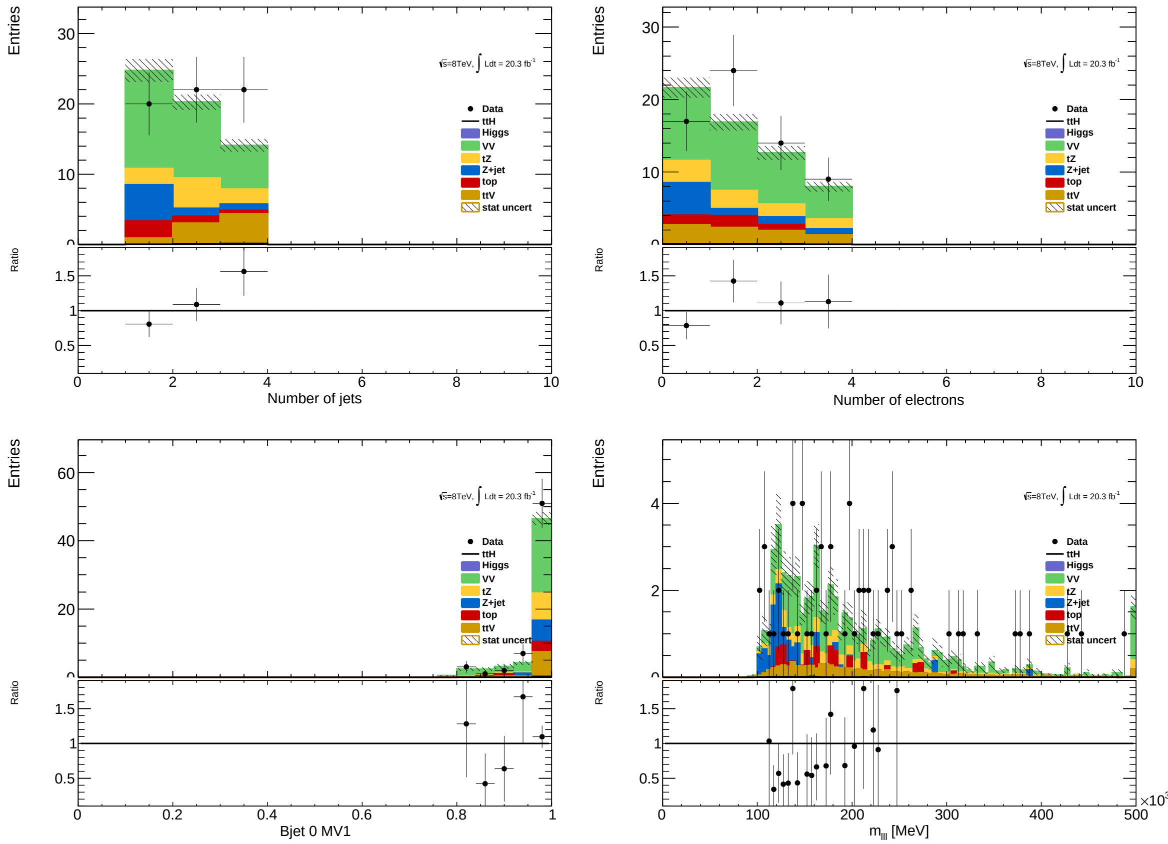

Figure 8.3: $W^{\pm}Z + b$ validation region: NJet, NElec, BJet MV1 and Mass Variables

in the 3-jet bin. Importantly, also the tagged jet composition is also similar to the composition in the $V + b$ analysis, already measured by ATLAS and discussed above.

	Bottom	Charm	Light
$W^{\pm}Z + b$ VR 1 Jet	0.25 ± 0.03	0.054 ± 0.04	0.20 ± 0.03
$W^{\pm}Z + b$ VR 2 Jet	0.34 ± 0.04	0.052 ± 0.06	0.13 ± 0.03
$W^{\pm}Z + b$ VR 3 Jet	0.40 ± 0.07	0.041 ± 0.07	0.18 ± 0.04
$3l$ SR	0.43 ± 0.14	0.038 ± 0.17	0.18 ± 0.11

Table 8.2: Truth Origin of highest energy b-tagged jet in the $W^{\pm}Z + b$ VR and $3l$ SR

8.2.2 ZZ Uncertainty

In order to investigate the MC agreement with data in the ZZ case, two validation regions similar to the $W^{\pm}Z$ case are defined. Firstly, a 4 lepton ZZ region is constructed using the object selections for the 4-lepton channel and requiring exactly two pairs of opposite sign-same flavour leptons with a di-lepton invariant mass within 10 GeV/$c^2$of the Z mass. Additionally, the $ZZ+b$ process is investigated directly using a similar validation region which again requires exactly two Z-candidate lepton pairs as well as at least 1 b-tagged jet. Some kinematic distributions are shown in Figures 8.4 and 8.5, and particular attention should be paid to the NJet spectrum which shows good data-MC agreement in the high-jet bins, with a slight discrepancy in the 1-jet bin. The agreement for the region with at least 2 jets yields confidence in the NJet MC modelling in this region which lies close to the 4-lepton signal region.

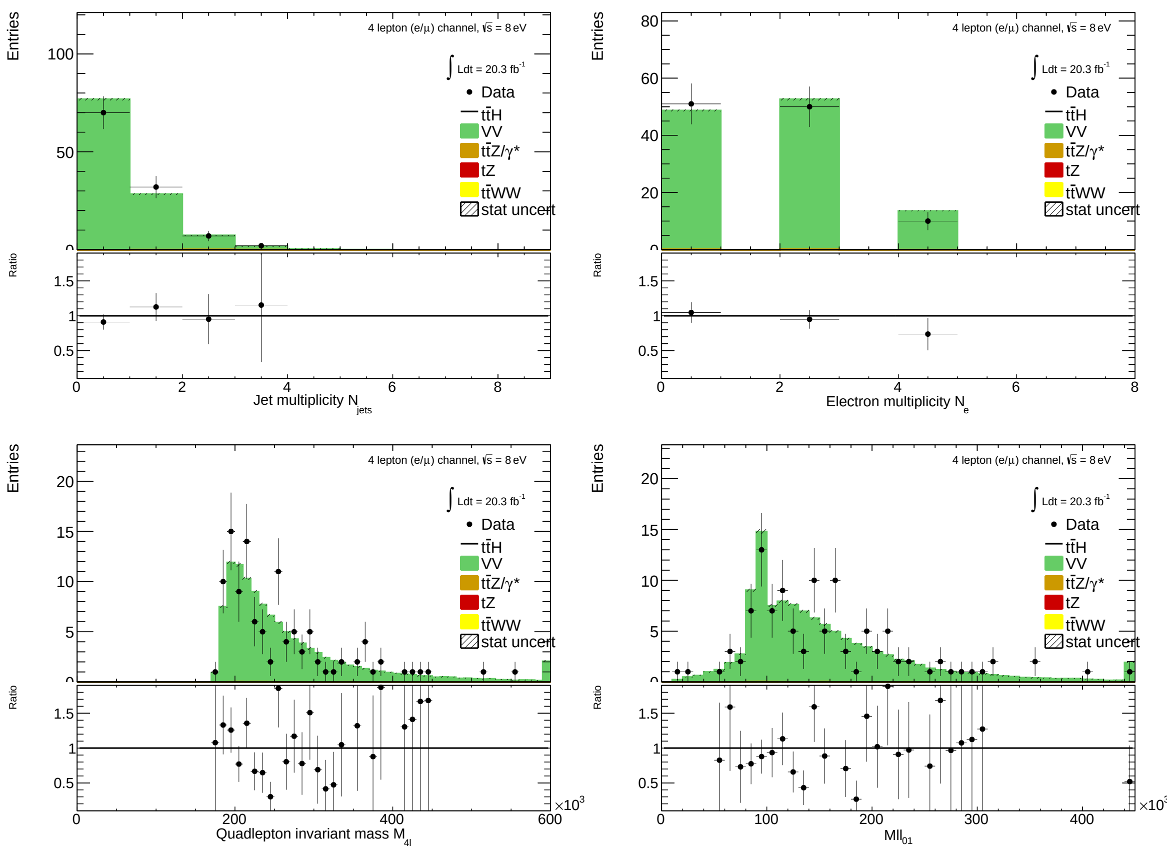

Figure 8.4: Jet-inclusive 4-lepton ZZ validation region using the $t\bar{t}H$ lepton identification and momentum cuts

Recall that in the $W^{\pm}Z$ case an overall systematic uncertainty of 50% was assigned to cover the MC modeling. Based on the study of the ZZ and $ZZ+b$ validation regions and the overall agreement noted with the $Z+b$ analysis, we expect a similar error to be appropriate in the ZZ case. A similar truth origin study is undertaken in MC to demonstate a similar b-jet origin to the $W^{\pm}Z$ case. The true origin of the leading (highest energy) b-tagged jet is shown in Table 8.3 for the 4-lepton signal

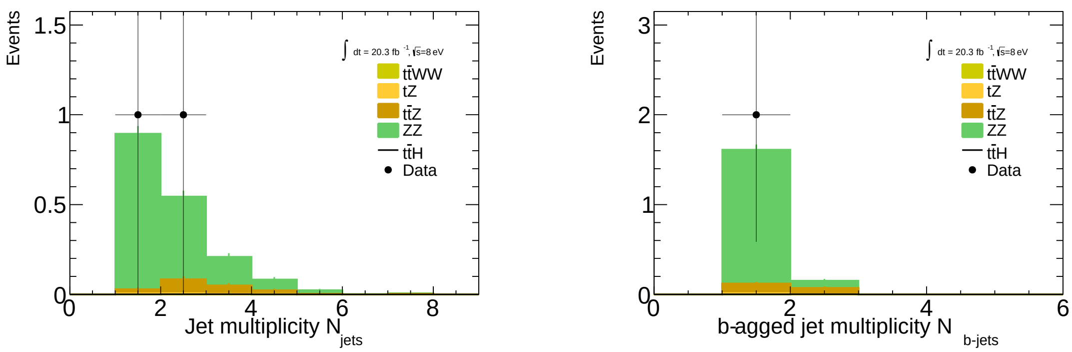

Figure 8.5: $ZZ + b$ validation region using the $t\bar{t}H$ lepton identification and momentum cuts

region as well as the $ZZ + b$ validation region described above divided into jet bins. It can be seen that in case, as it was in the $W^{\pm}Z$ case above, the true origin of the b-jet in $ZZ + b$ is dominated by c and b.

	Bottom	Charm	Light
$ZZ + b$ VR 1 Jet	0.50 ± 0.02	0.21 ± 0.01	0.18 ± 0.01
$ZZ + b$ VR 2 Jet	0.25 ± 0.02	0.12 ± 0.01	0.11 ± 0.01
$ZZ + b$ VR 3 Jet	0.085 ± 0.014	0.040 ± 0.011	0.036 ± 0.011
$4l$ SR	0.020 ± 0.008	0.025 ± 0.008	0.014 ± 0.005

Table 8.3: Truth Origin of highest energy b-tagged jet in the $ZZ + b$ VR and $4l$ SR

8.3 Charge-Misidentification Background

Charge-misidentification contributes to the background for 2l SS case and only for flavor channels, which include electrons. The same-sign require is useful in removing large SM opposite sign-backgrounds, but because of their size even small charge mis-identification rates result in contamination in same-sign regions. For the 2l SS signal regions and low NJet control regions, charge-misidentification backround arise primarily from $t\bar{t}$di-lepton events with a smaller contribution from leptonic Z decays.

In general, charge-misidentification can arise in two ways. The first occurs for ultra-high energy electrons and muons, which leave tracks in the detector that are too straight for the fit detetermine the direction of curvature with high confidence. This type of charge mis-identification is not a concern to the $t\bar{t}H$ multi-lepton analysis, as most of the leptons have momentum > 150 GeV/c. The second source of charge misidentification is from 'tridents', which only occurs for electrons, because their low mass allows for high rate bremmstrahlung in the detector material. In some cases, after an electron releases a photon through bremstrahlung, the photon may convert nearby resulting in three electron tracks. The reconstruction algorithms may sometimes match the wrong track to the calorimeter energy deposit, resulting in a possible charge mis-identifcation. As discussed in the selection, tight track-cluster geometric and energy matching requirements are applied on the electron candidates to reduce the overall rate and the electron acceptance is narrowed to ($|\eta| < 1.37$), since most of the material is concentrated more forward in the detector. For this reason, muon charge-misidentification is considered neglibible for this analysis.

We estimate the contribution of charge-misidentification events in our 2l SS signal regions and relevant control regions by appling a weight per electron in the opposite-sign region with otherwise same cuts. The weight is related to the charge-misidentification rates and is estimated using a likelihood method in the opposite-sign and same-sign $Z \to ee$ control regions. The rate measured from these control regions is binned in electron $p_{\mathrm{T}}$and η, to account for dependencies in these variables. The method, validations and associated errors are discussed in detail in the following sub-sections.

8.3.1 Likelihood Method

The number of reconstruted same-sign (N_{ss}) and opposite sign (N_os) $Z \to ee$ events are related to number of produced $Z \to ee$ opposite sign events (N) via factors related to the charge mis-identification rate. For a single per-electron charge mis-identification rate ($ilon$, these quantities are related as follows (with the assumption that $ilon$ is very small:

- $N^{os} = (1 - 2ilon + 2ilon^2)N$ opposite-sign events,
- $N^{ss} = 2ilon(1 - ilon)N \simeq 2ilonN$ same-sign events,

Knowing $ilon$, the charge-misidentification rate, and supposing we can have a different rate per-electron, it is possible to estimate the number of same-sign events from the number of opposite sign events.

- $N^{ss} = \frac{ilon_i + ilon_j - 2ilon_i ilon_j}{1 - ilon_i - ilon_j + 2ilon_i ilon_j} N^{os}$ for the ee channel,
- $N^{ss} = \frac{ilon}{1 - ilon} N^{os}$ for the $e\mu$ channel,

where $ilon_i$ and $ilon_j$ are the charge mis-identification rates for the two different electrons.

Althought it is impossible from a typical same-sign $Z \to ee$ to know which electron's charge was mis-identified, we can use a likelihood method over the whole sample to measure charge mis-identification rate ($ilon$) depends on the electron $p_{\mathrm{T}}$and η. The likelihood method assumes that the mis-identification rates of the electron charge are independent for different pseudorapidity regions. Therefore, the probability to have a number of same-sign events (N_{ss}^{ij}) with electrons in $|\eta|$ region i and j can be written as a function of the number of events N^{ij} as follows:

$$N_{ss}^{ij} = N^{ij}(ilon_i + ilon_j). \tag{8.1}$$

If all the same-sign events in the Z peak are produced by charge mis-identification, then N_{ss}^{ij} is described by a Poisson distribution:

$$f(k, \lambda) = \frac{\lambda^k e^{-\lambda}}{k!}, \tag{8.2}$$

where k is the observed number of occurrences of the event, i.e. $k = N_{ss}^{ij}$, and λ is the expected number, i.e. $\lambda = N^{ij}(ilon_i + ilon_j)$. Thus, the probability for both electrons to produce a charge mis-identification is expressed by:

$$P(ilon_i, ilon_j | N_{ss}^{ij}, N^{ij}) = \frac{[N^{ij}(ilon_i + ilon_j)]^{N_{ss}^{ij}} e^{-N^{ij}(ilon_i + ilon_j)}}{N_{ss}^{ij}!}. \tag{8.3}$$

The likelihood L for all the events is obtained by evaluating all the $|\eta|$ combinations:

$$L(ilon | N_{ss}, N) = \prod_{i,j} \frac{[N^{ij}(ilon_i + ilon_j)]^{N_{ss}^{ij}} e^{-N^{ij}(ilon_i + ilon_j)}}{N_{ss}^{ij}!}, \tag{8.4}$$

where the rates $ilon_i$ and $ilon_j$ can be obtained by minimizing the likelihood function. In this process, the $-\ln L$ is used in order to simplify and make easier the minimization. Terms which do not depend on the rates $ilon_i$ and $ilon_j$ are removed in this step. This way, the final function to minimize is given by the following expression:

$$-\ln L(ilon | N_{ss}, N) \approx \sum_{i,j} \ln[N^{ij}(ilon_i + ilon_j)] N_{ss}^{ij} - N^{ij}(ilon_i + ilon_j). \tag{8.5}$$

The events are selected within the Z peak and stored –with the electron order by $|\eta|$– in two triangular matrices: one for the same-sign events N_{ss}^{ij}, and the other one for all events N^{ij}. The likelihood method takes into account electron pairs with all $|\eta|$ combinations, which allows to use the full available statistics getting therefore lower statistical uncertainties. Moreover, it does not bias the kinematical properties of the electrons, compared to other methods like tag-and-probe.

The likelihood method can be easily extended to measure the charge mis-identification rates as a function of two parameters. In this study, the interest lies not only on the measurement of the rates as a function of the pseudorapidity, but also transverse momentum. Thus, the probability to find a same-sign event given the rates for each electron is $(ilon_{i,k} + ilon_{j,l})$, where the two indices represent binned $|\eta|$- and p_{T}-dependence. Thus, the Eq. 8.5 transforms into

$$-\ln L(ilon | N_{ss}, N) \approx \sum_{i,j,k,l} \ln[N^{ij,kl}(ilon_{i,k} + ilon_{j,l})] N_{ss}^{ij,kl} - N^{ij,kl}(ilon_{i,k} + ilon_{j,l}). \tag{8.6}$$

The likelihood method uses only Z *signal* events. Therefore, background coming from other processes where the dilepton invariant mass corresponds to the one of the Z boson needs to be subtracted. The background subtraction is done using a simple side-band method. This method consists in dividing the Z invariant mass in three regions, i.e. A, B and C, where B is the central region corresponding to the Z peak. The number of events is counted in the regions on the sides of the peak, i.e. n_A and n_C, and removed from the total number of events in the peak region B, n_B. This way, the number of signal events N_Z is given by

$$N_Z = n_B - \frac{n_A + n_C}{2}. \tag{8.7}$$

Once the background has been subtracted, the likelihood method can be applied. MINUIT is used for the minimization and MIGRAD to compute the uncertainty on these rates.

8.3.2 Results

The charge mis-identification rate is calculated in 7 $|\eta|$ bins [0.0, 0.6, 1.1, 1.37, 1.52, 1.7, 2.3, 2.47] by 4 p_{T}bins [15,60,90,130,1000]. For p_{T}bins above 130 GeV/c, the Z dataset becomes too small and the rates are calculated using $t\bar{t}$MC, scaled by the data-MC ratio of the rates in the lower p_{T}bins, [90-130] GeV/c. Figure 8.6 shows the extracted rates in all bins.

To validate the likelihood approach, we apply the full method to the Z MC samples (extracting rates via a likelihood fit and applying them to opposite sign events) and compare to the MC predicted number of same-sign events. The invariant mass of the Z from our charge mis-identification and directly from the MC can be seen on Figure 8.7. In the simulated Z samples, the number of same-sign Z events is 5 049 while the estimation is 5 031^{+375}_{-365}. The uncertainties combine both statistical systematic uncertainties, which are discussed in depth below. The validation gives compatible results within uncertainties.

8.3.3 Systematic and Statistical Uncertainties

Statistical uncertainties dominate the combined uncertainty on the charge mis-identification estimate. The statistical uncertainties come primarily from the size of the Z same-sign sample in data and are especially large for central, material-poor regions where the charge mis-identification rate is extremely low. Additionaly systematic uncertainties are included for a comparison between the positron and electron rate, the per-bin MC closure test discussed above in the Results section, and for the effect of varying the invariant mass window used for the background subtraction for three different cases. The high p_{T}extrapolation induces a statistical error only in the last p_{T}bin. This bins is essentially irrelevant

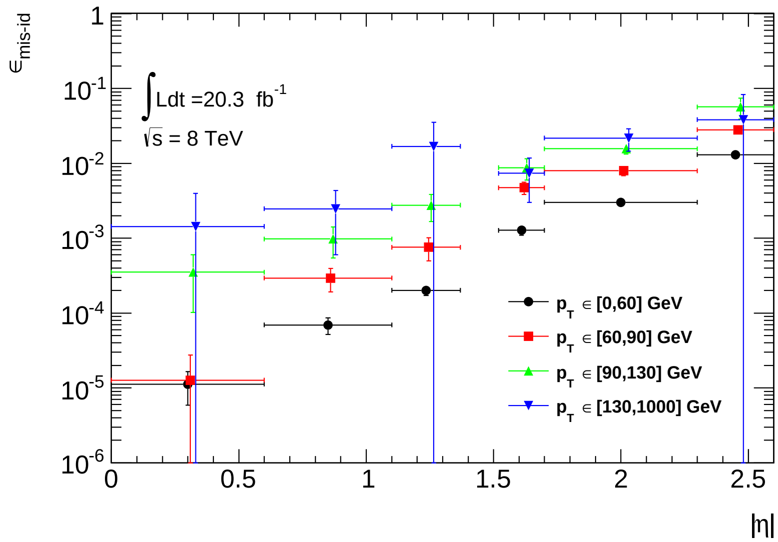

Figure 8.6: Electron charge mis-identification rates measured in data with the likelihood method on Z events (black points, red squares and blue triangles) as a function of $|\eta|$ and parametrized in p_{T}. The full 2012 dataset has used to estimate the rates below 130 GeV. Above this value, the charge mis-identification rates have been estimated by extrapolating the rates in the region where the $p_{\mathrm{T}} \in [90, 130]$ GeV with a p_{T} dependent factor extracted from simulated $t\bar{t}$ events (green triangles). Statistical and systematic uncertainties have been included in this plot.

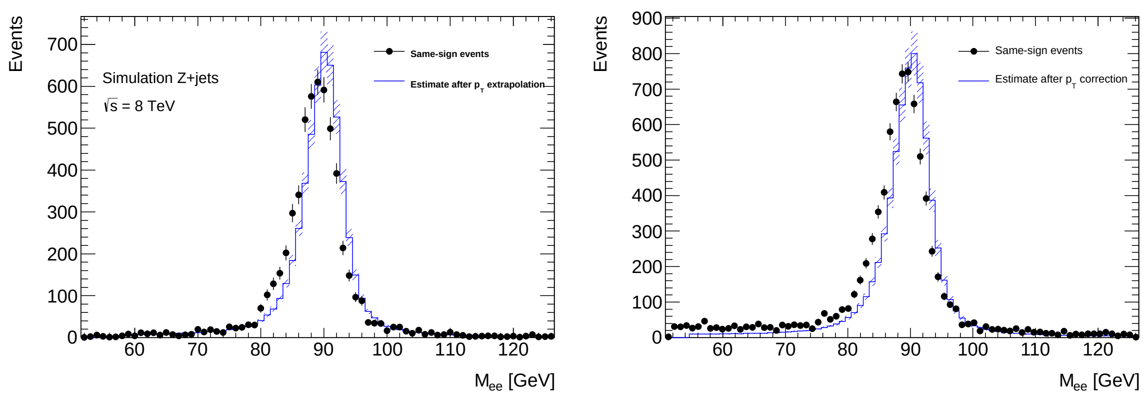

Figure 8.7: Closure test on simulated $Z \rightarrow e^+e^- + jets$ events (a) and data (b). The black circles show the distribution of same-sign events while the blue histograms show the distribution of the reweighted opposite-sign events together with the statistical and systematic uncertainties. The distributions are not expected to overlay exactly, due to the loss of energy of the trident electrons for the same-sign peak.

to the energy scales considered in this analysis. Figure 8.8 shows the relative bin uncertanties for all rate bins.

We apply the rates to estimate the charge mis-identification background in the 2l SS signal regions,

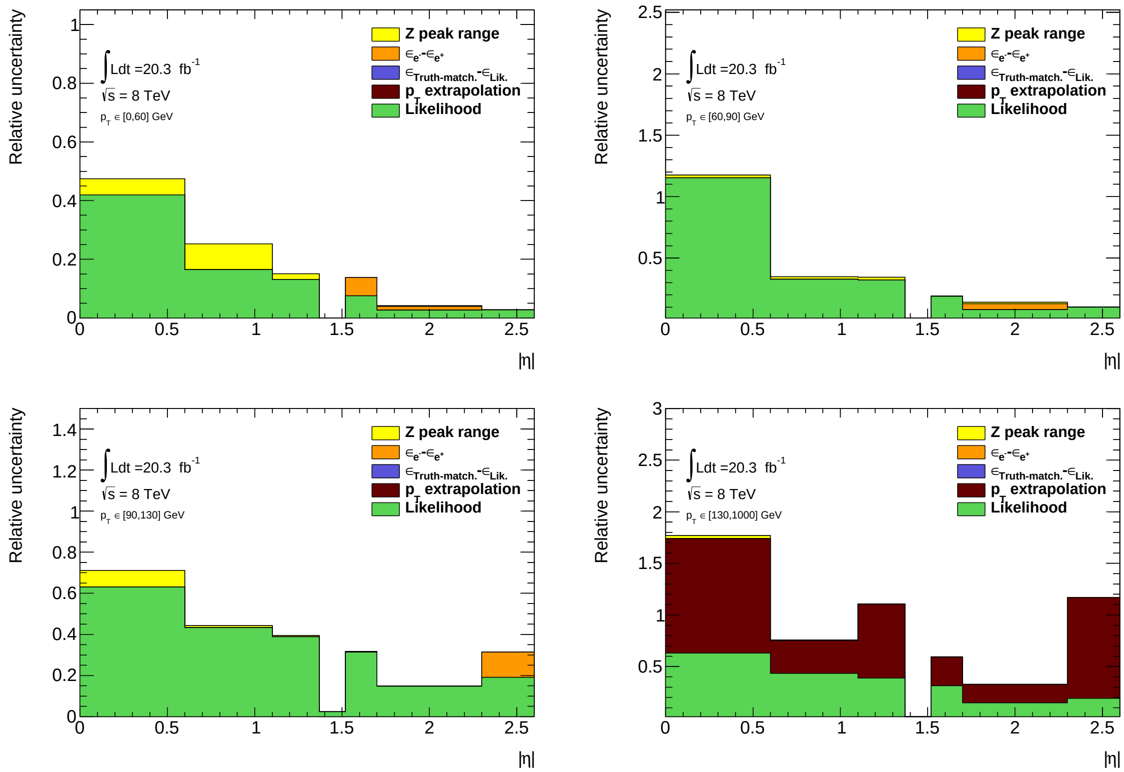

Figure 8.8: Relative systematic uncertainty contributions on the charge mis-identification rate, for different bins in p_{T} and $|\eta|$. Tight++ electrons have been used to produce this plot.

and find $\sim$ 25% contamination in the $e^{\pm}e^{\pm}$ regions and a $\sim$ 10% contribution to the $e^{\pm}\mu^{\pm}$ regions with a 10% systematic error overall. The low overall error can be attributed to the fact that the statistical error is lowest where the bulk of charge misidentifications occur.

8.4 Fake Lepton Backgrounds

Fake Leptons, from the mis-identification of jets as either electrons or muons, primarily arise from $t\bar{t}$events in the 2l SS, 3l and 4l channels. Smaller contributions come from Z+jet events. These backgrounds are sub-dominant but important in the 2lSS and 3l channels but extremely small in the 4l channels. To estimate these backgrounds, we employ data-driven control regions near the signal region with fewer jets that are fake enriched and control regions with reversed cuts. These regions are studied using MC and are shown to be good models for fake backgrounds in the signal region, because they possess similar fake origin and composition. These truth studies suggest that both electrons and muons arise overwhelimingly from b-quark originated jets.

The general method for all channels is to define a reversed object selection region (usually isolation) for each lepton flavor with otherwise identical signal region selection (N^e_{CR}, N^{μ}_{CR}). This region is fake-dominated with small contributions from prompt backgrounds, which are subtracted from the data. The total number of fake events in this region is then scaled by a transfer factor (θ) to estimate the number of fake events of the appropriate flavor in the siganl region. The transfer factor is defined in Equations 8.8 and the simple formula for determining fakes is defined in Equations 8.9. 'x' refers to any combination of tight muons and/or electrons, 'd' refers to anti-identified electrons, and 'p' refers to anti-identified muons.

$$\theta_e = \frac{N_{xe}}{N_x d}, \theta_\mu = \frac{N_{x\mu}}{N_{xp}} \tag{8.8}$$

$$N_{fake} = \theta_e * N^e_{CR} + \theta_\mu * N^\mu_{CR} \tag{8.9}$$

This approach factorizes the background model into two separate measurements. N_{CR} is sensitive the overall $t\bar{t}$production rate, especially in the presence of additional jets from QCD ratio, as well as the object-level misidentification of a jet as a lepton. The transfer factor θ is sensitive to only the object level properties of the mis-identified jet, and in particular only the variables which are reversed in the anti-tight indentification.

The transfer factor is obtained in a different way for each channel, due to unique issues with statistics and contamination, but each method relies heavily on the data-based control regions with fewer jets. Figure 8.9 shows a truth study of the stability of the transfer factor for the 2l SS and 3l cases as a function of the number of jets in the event for events with one-btagged jet. This suggest that the regions with fewer jets are a good model of the fakes in the signal regions with more jets and is expected because of the homogeneity of origin of the fakes across all jet bins.

The details of the methods for each channel are discussed in depth in the following sections. For all methods, the overall systematic uncertainty on the normalization of the fake estimate is in the range 30%-50% and arise primarily from statistics and the closure on assumptions used to obtain the transfer factor.

Because these methods do provide a per-object transfer-factor that depends on the properties of the faking object, we must use the MC to model the shapes of the fake kinematic distributions in the signal regions. This is not an essential issue, since the analysis only cconsiders only the total number of events in each signal region in the final measurement of $t\bar{t}H$ production.

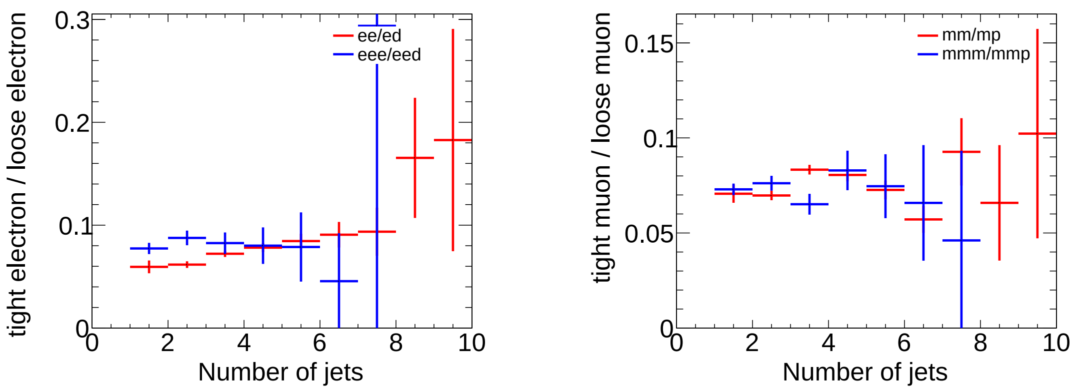

Figure 8.9: Ratios of regions with tight and loose leptons in 2-lepton and 3-lepton channels

8.4.1 2l SS Fakes

The 2l SS fake method follows the procedure outlined in general above. We define anti-tight electron and muon control regions with reversed particle identification criteria for each signal region, including the 6 flavor and jet-counting sub regions. The anti-tight muon and electron criteria are provided below:

- **e**lectron: fails to verify the Verytight likelihood operating point, but still verifies the Veryloose opoperating point. fails relative tracking and calorimeter isolation, $\mathrm{E}_T^{rel} > 0.05$ and $\mathrm{p}_T^{rel} > 0.05$.
- **m**uon: 6 GeV/c< p_{T} < 10 GeV/c

The electron and muon transfer factors, θ_e and θ_μ, are calculated in the region with signal region selection but fewer jets, $NJet == 2$ or $NJet == 3$ and are defined as the ratio of the number of events for two fully identified leptons to the number of events with one fully identified lepton and one anti-identified lepton, after the prompt and charge mis-identification bakgrounds are subtracted. Only same-flavor channels are used to ensure that muon and electron transfer factors maybe estimated separately: on every region, the prompt and charge-misidentification backgrounds are subtracted from the data.

$$\theta_e = \frac{N_{ee}}{N_{ed}} = \frac{N_{ee}^{Data} - N_{ee}^{\mathrm{Prompt}\ SS} - N_{ee}^{\mathrm{Q}MisId}}{N_{ed}^{Data} - N_{ed}^{\mathrm{Prompt}\ SS} - N_{ed}^{\mathrm{Q}MisId\ MC}} \tag{8.10}$$

$$\theta_m = \frac{N_{\mu\mu}}{N_{\mu p}} = \frac{N_{\mu\mu}^{Data} - N_{\mu\mu}^{\mathrm{Prompt}\ SS}}{N_{\mu p}^{Data} - N_{\mu p}^{\mathrm{Promt}\ SS}} \tag{8.11}$$

Figures show the plots of NJet used for the regions used in the transfer factor extrapolation. Other kintematic distributions are not shown for brevity

8.4.2 3l Fakes

The 3l fake method follows the same general strategy as above. Hoewver, the low NJet region has too low statistics

8.4.3 4l Fakes

CHAPTER 9

Conclusions

9.1 Higgs Results in Review

9.2 Prospects for Future

Bibliography

[1] S. L. Glashow, *Partial-symmetries of weak interactions*, Nucl. Phys. **2**2 (1961) no. 4, 579. 2.1.1

[2] S. Weinberg, *A Model of Leptons*, Phys. Rev. Lett. **1**9 (1967) 1264. 2.1.1

[3] A. Salam and J. C. Ward, *Gauge theory of elementary interactions*, Phys. Rev. **1**36 (1964) 763–768. 2.1.1

[4] S. Weinberg, *Non-abelian gauge theories of the strong interactions*, Phys. Rev. Lett. **3**1 (1973) 494–497. 2.1.1

[5] D. J. Gross and F. Wilczek, *Ultraviolet behavior of non-abelian gauge theories*, Phys. Rev. Lett. **30** (1973) 1343–1346. 2.1.1

[6] G. 't Hooft and M. Veltman, *Regularization and renormalization of gauge fields*, Nuclear Physics B **44** (1972) 189 – 213. 2.1.1

[7] P. W. Higgs, *Broken symmetries and the masses of gauge bosons*, Phys. Rev. Lett. **1**3 (1964) 508. 2.1.2

[8] P. W. Higgs, *Spontaneous symmetry breakdown without massless bosons*, Phys. Rev. **1**45 (1966) 1156. 2.1.2

[9] F. Englert and R. Brout, *Broken Symmetry and the Mass of Gauge Vector Mesons*, Phys. Rev. Lett. **13** (1964) 321–322. 2.1.2

[10] The ALEPH, CDF, DØ, DELPHI, L3, OPAL, SLD Collaborations, the LEP Electroweak Working Group, the Tevatron Electroweak Working Group, and the SLD electroweak and heavy flavour groups, *Precision Electroweak Measurements and Constraints on the Standard Model*, CERN-PH-EP-2010-095 (2010) , arXiv:1012.2367 [hep-ex]. 2.1.3, 2.2

[11] M. Baak, M. Goebel, J. Haller, A. Hoecker, D. Kennedy, R. Kogler, K. Mnig, M. Schott, and J. Stelzer, *The electroweak fit of the standard model after the discovery of a new boson at the LHC*, The European Physical Journal C **7**2 (2012) no. 11, . `http://dx.doi.org/10.1140/epjc/s10052-012-2205-9`. 2.1.3

[12] J. C. Collins, D. E. Soper, and G. Sterman, *Factorization for short distance hadron-hadron scattering*, Nuclear Physics B **261** (1985) 104 – 142. 2.2

[13] CERN, . CERN, Geneva, 1984. 2.2

[14] LHC Higgs Cross Section Working Group, S. Dittmaier, C. Mariotti, G. Passarino, and R. Tanaka (Eds.), *Handbook of LHC Higgs Cross Sections: 2. Differential Distributions*, CERN-2012-002 (CERN, Geneva, 2012) , arXiv:1201.3084 [hep-ph]. 2.2

[15] *Updated coupling measurements of the Higgs boson with the ATLAS detector using up to 25 fb^{-1} of proton-proton collision data*, Tech. Rep. ATLAS-CONF-2014-009, CERN, Geneva, Mar, 2014. 2.2.1

[16] CMS Collaboration Collaboration, *Precise determination of the mass of the Higgs boson and studies of the compatibility of its couplings with the standard model*, Tech. Rep. CMS-PAS-HIG-14-009, CERN, Geneva, 2014. 2.2.1

[17] ATLAS Collaboration Collaboration, G. Aad et al., *Measurement of the Higgs boson mass from the $H \to \gamma\gamma$ and $H \to ZZ^* \to 4\ell$ channels with the ATLAS detector using 25 fb^{-1} of pp collision data*, arXiv:1406.3827 [hep-ex]. 2.2.1

[18] *Evidence for the spin-0 nature of the Higgs boson using {ATLAS} data*, Physics Letters B **7**26 (2013) no. 13, 120 – 144. http://www.sciencedirect.com/science/article/pii/S0370269313006527. 2.2.1

[19] S. Dawson, A. Gritsan, H. Logan, J. Qian, C. Tully, et al., *Working Group Report: Higgs Boson*, arXiv:1310.8361 [hep-ex]. 2.2.2

[20] O. Eberhardt, G. Herbert, H. Lacker, A. Lenz, A. Menzel, et al., *Impact of a Higgs boson at a mass of 126 GeV on the standard model with three and four fermion generations*, Phys.Rev.Lett. **1**09 (2012) 241802, arXiv:1209.1101 [hep-ph]. 2.2.2

[21] M. Carena, S. Gori, N. R. Shah, C. E. Wagner, and L.-T. Wang, *Light Stops, Light Staus and the 125 GeV Higgs*, JHEP **1**308 (2013) 087, arXiv:1303.4414. 2.2.2

[22] N. Arkani-Hamed, K. Blum, R. T. D'Agnolo, and J. Fan, *2:1 for Naturalness at the LHC?*, JHEP **1**301 (2013) 149, arXiv:1207.4482 [hep-ph]. 2.2.2

[23] D. Carmi, A. Falkowski, E. Kuflik, and T. Volansky, *Interpreting LHC Higgs Results from Natural New Physics Perspective*, JHEP **1**207 (2012) 136, arXiv:1202.3144 [hep-ph]. 2.2.2

[24] G. Degrassi, S. Di Vita, J. Elias-Miro, J. R. Espinosa, G. F. Giudice, et al., *Higgs mass and vacuum stability in the Standard Model at NNLO*, JHEP **1**208 (2012) 098, arXiv:1205.6497 [hep-ph]. 2.2.2

[25] L. Evans and P. Bryant, *LHC Machine*, JINST **3** (2008) no. 08, S08001. 3.1

[26] T. S. Pettersson and P. Lefevre, *The Large Hadron Collider: conceptual design.*, Tech. Rep. CERN-AC-95-05 LHC, CERN, Geneva, Oct, 1995. https://cdsweb.cern.ch/record/291782. 3.1

[27] T. Linnecar et al., *Hardware and Initial Beam Commissioning of the LHC RF Systems. oai:cds.cern.ch:1176380*, Tech. Rep. LHC-PROJECT-Report-1172. CERN-LHC-PROJECT-Report-1172, CERN, Geneva, Oct, 2008. https://cdsweb.cern.ch/record/1176380. 3.1

[28] ATLAS Collaboration, *The ATLAS Experiment at the CERN Large Hadron Collider*, JINST **3** (2008) S08003. 3.1

[29] The CMS Collaboration, *The CMS experiment at the CERN LHC*, Journal of Instrumentation **3** (2008) no. 08, S08004. 3.1

[30] The LHCb Collaboration, *The LHCb Detector at the LHC*, Journal of Instrumentation **3** (2008) no. 08, S08005. 3.1

[31] The ALICE Collaboration, *The ALICE experiment at the CERN LHC*, Journal of Instrumentation **3** (2008) no. 08, S08002. http://stacks.iop.org/1748-0221/3/i=08/a=S08002. 3.1

[32] A. Team, *The four main LHC experiments*, Jun, 1999. 3.1

[33] ATLAS Collaboration Collaboration, G. Aad et al., *Search for $H \to \gamma\gamma$ produced in association with top quarks and constraints on the Yukawa coupling between the top quark and the Higgs boson using data taken at 7 TeV and 8 TeV with the ATLAS detector*, arXiv:1409.3122 [hep-ex]. 5

[34] *Search for the Standard Model Higgs boson produced in association with top quarks and decaying to $b\bar{b}$ in pp collisions at $\sqrt{s}$ = 8 TeV with the ATLAS detector at the LHC*, Tech. Rep. ATLAS-CONF-2014-011, CERN, Geneva, Mar, 2014. 5

[35] ATLAS Collaboration, G. Aad et al., *Improved luminosity determination in pp collisions at $\sqrt{s}$ = 7 TeV using the ATLAS detector at the LHC*, Eur.Phys.J. **C**73 (2013) 2518, arXiv:1302.4393 [hep-ex]. 6.1.1

[36] CERN, . CERN, Geneva, 2012. 6.1.1

[37] ATLAS Collaboration Collaboration, G. Aad et al., *The ATLAS Simulation Infrastructure*, Eur.Phys.J. **C**70 (2010) 823–874, arXiv:1005.4568 [physics.ins-det]. 6.2

[38] GEANT4 Collaboration, S. Agostinelli et al., *GEANT4: A Simulation toolkit*, Nucl.Instrum.Meth. **A**506 (2003) 250–303. 6.2

[39] LHC Higgs Cross Section Working Group Collaboration, S. Heinemeyer et al., *Handbook of LHC Higgs Cross Sections: 3. Higgs Properties*, arXiv:1307.1347 [hep-ph]. 6.2.1

[40] M. V. Garzelli, A. Kardos, and Z. Trocsanyi, *$t\bar{t}$ + hard X hadroproduction with PowHel*, PoS **L**L2012 (2012) 057. 6.2.1

[41] T. Sjostrand, S. Mrenna, and P. Z. Skands, *A Brief Introduction to PYTHIA 8.1*, Comput.Phys.Commun. **178** (2008) 852–867, arXiv:0710.3820 [hep-ph]. 6.2.1

[42] H.-L. Lai, M. Guzzi, J. Huston, Z. Li, P. M. Nadolsky, et al., *New parton distributions for collider physics*, Phys.Rev. **D**82 (2010) 074024, arXiv:1007.2241 [hep-ph]. 6.2.1

[43] M. L. Mangano, M. Moretti, F. Piccinini, R. Pittau, and A. D. Polosa, *ALPGEN, a generator for hard multiparton processes in hadronic collisions*, JHEP **0**307 (2003) 001, arXiv:hep-ph/0206293 [hep-ph]. 6.2.2

[44] F. Maltoni and T. Stelzer, *MadEvent: Automatic event generation with MadGraph*, JHEP **0**302 (2003) 027, arXiv:hep-ph/0208156 [hep-ph]. 6.2.2

[45] B. P. Kersevan and E. Richter-Was, *The Monte Carlo event generator AcerMC versions 2.0 to 3.8 with interfaces to PYTHIA 6.4, HERWIG 6.5 and ARIADNE 4.1*, Comput.Phys.Commun. **184** (2013) 919–985, arXiv:hep-ph/0405247 [hep-ph]. 6.2.2

[46] P. M. Nadolsky, H.-L. Lai, Q.-H. Cao, J. Huston, J. Pumplin, et al., *Implications of CTEQ global analysis for collider observables*, Phys.Rev. **D78** (2008) 013004, arXiv:0802.0007 [hep-ph]. 6.2.2

[47] S. Frixione, P. Nason, and C. Oleari, *Matching NLO QCD computations with Parton Shower simulations: the POWHEG method*, JHEP **0711** (2007) 070, arXiv:0709.2092 [hep-ph]. 6.2.2

[48] T. Gleisberg, S. Hoeche, F. Krauss, M. Schonherr, S. Schumann, et al., *Event generation with SHERPA 1.1*, JHEP **0902** (2009) 007, arXiv:0811.4622 [hep-ph]. 6.2.2

[49] A. Martin, W. Stirling, R. Thorne, and G. Watt, *Parton distributions for the LHC*, Eur.Phys.J. **C63** (2009) 189–285, arXiv:0901.0002 [hep-ph]. 6.2.2, 8.1

[50] *Electron efficiency measurements with the ATLAS detector using the 2012 LHC proton-proton collision data*, Tech. Rep. ATLAS-CONF-2014-032, CERN, Geneva, Jun, 2014. 7.4

[51] *Preliminary results on the muon reconstruction efficiency, momentum resolution, and momentum scale in ATLAS 2012 pp collsion data*, Tech. Rep. ATLAS-CONF-2013-088, CERN, Geneva, February, 2013. 7.5

[52] M. Cacciari, G. P. Salam, and G. Soyez, *The Anti-k(t) jet clustering algorithm*, JHEP **0804** (2008) 063, arXiv:0802.1189 [hep-ph]. 7.6

[53] M. Garzelli, A. Kardos, C. Papadopoulos, and Z. Trocsanyi, *$t\bar{t}W^{\pm}$ and $t\bar{t}Z$ Hadroproduction at NLO accuracy in QCD with Parton Shower and Hadronization effects*, JHEP **1211** (2012) 056, arXiv:1208.2665 [hep-ph]. 8.1

[54] J. M. Campbell and R. K. Ellis, *$t\bar{t}W^{+-}$ production and decay at NLO*, JHEP **1207** (2012) 052, arXiv:1204.5678 [hep-ph]. 8.1

[55] Campbell, John and Ellis, R. Keith and Röntsch, Raoul, *Single top production in association with a Z boson at the LHC*, Phys.Rev. **D87** (2013) 114006, arXiv:1302.3856 [hep-ph]. 8.1

[56] ATLAS Collaboration Collaboration, G. Aad et al., *Measurement of WZ production in proton-proton collisions at $\sqrt{s} = 7$ TeV with the ATLAS detector*, Eur.Phys.J. **C72** (2012) 2173, arXiv:1208.1390 [hep-ex]. 8.2

[57] ATLAS Collaboration Collaboration, G. Aad et al., *Measurement of ZZ production in pp collisions at $\sqrt{s} = 7$ TeV and limits on anomalous ZZZ and $ZZ\gamma$ couplings with the ATLAS detector*, JHEP **1303** (2013) 128, arXiv:1211.6096 [hep-ex]. 8.2

[58] ATLAS Collaboration Collaboration, G. Aad et al., *Measurement of the cross-section for W boson production in association with b-jets in pp collisions at $\sqrt{s}$ = 7 TeV with the ATLAS detector*, JHEP **1306** (2013) 084, arXiv:1302.2929 [hep-ex]. 8.2

[59] ATLAS Collaboration Collaboration, G. Aad et al., *Measurement of differential production cross-sections for a Z boson in association with b-jets in 7 TeV proton-proton collisions with the ATLAS detector*, arXiv:1407.3643 [hep-ex]. 8.2